Faculty Research, Scholarly, and Creative Activity

8-1-2021

Evaluation of the CAM6 Climate Model Using Cloud Observations at McMurdo Station, Antarctica

Jackson Yip
San Jose State University

Minghui Diao
San Jose State University, minghui.diao@sjsu.edu

Tyler Barone
San Jose State University

Israel Silber
Pennsylvania State University

Andrew Gettelman
National Center for Atmospheric Research

Follow this and additional works at: https://scholarworks.sjsu.edu/faculty_rsca

Recommended Citation

Evaluation of the CAM6 Climate Model Using Cloud Observations at McMurdo Station, Antarctica

Jackson Yip[1], Minghui Diao[1] , Tyler Barone[1], Israel Silber[2] , and Andrew Gettelman[3]

[1]Department of Meteorology and Climate Science, San Jose State University, San Jose, CA, USA, [2]Department of Meteorology and Atmospheric Science, Pennsylvania State University, University Park, PA, USA, [3]National Center for Atmospheric Research, Boulder, CO, USA

Abstract A comparative analysis between observational data from McMurdo Station, Antarctica and the Community Atmosphere Model version 6 (CAM6) simulation is performed focusing on cloud characteristics and their thermodynamic conditions. Ka-band Zenith Radar (KAZR) and High Spectral Resolution Lidar (HSRL) retrievals are used as the basis of cloud fraction and cloud phase identifications. Radiosondes released at 12-h increments provide atmospheric profiles for evaluating the simulated thermodynamic conditions. Our findings show that the CAM6 simulation consistently overestimates (underestimates) cloud fraction above (below) 3 km in four seasons of a year. Normalized by total in-cloud samples, ice and mixed phase occurrence frequencies are underestimated and liquid phase frequency is overestimated by the model at cloud fractions above 0.6, while at cloud fractions below 0.6 ice phase frequency is overestimated and liquid-containing phase frequency is underestimated by the model. The cloud fraction biases are closely associated with concurrent biases in relative humidity (RH), that is, high (low) RH biases above (below) 2 km. Frequencies of correctly simulating ice and liquid-containing phase increase when the absolute biases of RH decrease. Cloud fraction biases also show a positive correlation with RH biases. Water vapor mixing ratio biases are the primary contributor to RH biases, and hence, likely a key factor controlling the cloud biases. This diagnosis of the evident shortfalls of representations of cloud characteristics in CAM6 simulation at McMurdo Station brings new insight in improving the governing model physics therein.

Plain Language Summary Global climate models (GCMs) historically struggle to accurately estimate the amounts and types of clouds over the polar regions. Cloud cover and thermodynamic phase directly influence Earth's radiation budget and the accuracy of future climate prediction. Particularly, Antarctic ice sheet is vulnerable to a changing climate through interactions with atmosphere and ocean, and the impacts of clouds are still not well understood. In this study, shortcomings of cloud representations in the CAM6 model were diagnosed by comparing with observational data (ground-based remote sensing and radiosondes), which encompassed a year of measurements at McMurdo Station, Antarctica. Cloud fraction and phase as well as thermodynamic variables were examined to identify model biases. The model overestimates cloud cover above 3 km and underestimates it below that altitude. In cases where cloud cover is greater than 60%, the model also produces excessively large percentages of liquid clouds. These model biases are well correlated with biases in relative humidity, which is further dominated by biases in water vapor concentrations. Thus, these findings indicate that improving representations of water vapor concentrations in the model is a key step toward improving the simulations of cloud characteristics in Antarctica.

1. Introduction

Clouds directly affect Earth's atmospheric radiation budget and climate feedbacks (Ramanathan et al., 1989; Webb et al., 2017; Zelinka et al., 2020). Simulating clouds is an intricate challenge for global climate models (GCMs). In pursuit of improving the fidelity of future climate prediction, a better understanding of cloud radiative effects and the environmental conditions for cloud formation is needed. To estimate cloud radiative effects, models must accurately represent physical processes occurring during cloud formation and evolution, in order to capture cloud microphysical properties (e.g., mass and number concentrations of cloud hydrometeors) and macrophysical properties (e.g., vertical and horizontal extent, cloud fraction) (Liou, 1992; Liou & Wittman, 1979). Therefore, systematic identification of these physical processes is one

Project Administration: Minghui Diao
Resources: Minghui Diao
Software: Jackson Yip
Supervision: Minghui Diao
Validation: Jackson Yip, Minghui Diao
Visualization: Jackson Yip, Minghui Diao, Tyler Barone
Writing – original draft: Jackson Yip, Minghui Diao
Writing – review & editing: Jackson Yip, Minghui Diao, Israel Silber, Andrew Gettelman

of the key steps for improving the representation of cloud characteristics and their interaction with other parts of the Earth system such as the cryosphere and oceans.

Accurate representation of polar clouds in GCMs is foundational to correctly estimate the rate of global warming, given that polar regions bear the brunt of accelerated tropospheric and oceanic warming due to anthropogenic climate change (Nicolas et al., 2017; Oppenheimer, 1998; Shepherd et al., 2004; Turner et al., 2006). Ground-based and spaceborne remote sensing observations are often used for analysis of cloud characteristics in the polar regions. For example, de Boer et al. (2009) used multi-year lidar, radar, radiometer and radiosonde data from two sites in northern Canada and Alaska and found that the characteristics of single-layer mixed-phase clouds, such as occurrence frequency, cloud-base height and thickness, vary with season and location. Mioche et al. (2015) analyzed satellite observations over the region of Svalbard archipelago and found seasonal and regional variabilities in mixed-phase cloud frequencies, with a minimum 30% frequency in winter and 50% in other reasons, and a higher frequency in the Svalbard region than the rest of the Arctic region. Hemispheric comparisons between Antarctic and Arctic stratiform mixed-phase clouds at two research sites showed that McMurdo, Antarctica has a higher supercooled liquid fraction at a given cloud top temperature than Utqiaġvik (formerly Barrow) site in the North Slope of Alaska (D. Zhang, Vogelmann, et al., 2019). Model representation of cloud thermodynamic phases and cloud cover in the polar regions is influenced by numerous parameterization schemes (e.g., Hines et al., 2019; Listowski and Lachlan-Cope, 2017). A previous study of M. Zhang, Liu, et al., 2019 investigated the sensitivity of low-level mixed-phase clouds to various parameterizations in Community Atmosphere Model Version 5 (CAM5). They found that the Wegener-Bergeron-Findeisen (WBF) process has a significant effect on the transition from liquid to ice phase.

The Antarctic region, in particular, is of high interest for validation of GCMs. The West Antarctic Ice Sheet (WAIS), currently the second largest contributor to sea level rise following the Greenland Ice Sheet (Martin et al., 2019; Shepherd et al., 2004), has seen ice degradation at an accelerated rate in the presence of strong marine air surge into the region. Furthermore, with potentially warmer oceans (Martin et al., 2019) and amplified high-pressure ridge (Nicolas et al., 2017) into the future, resultant accelerated melting is a possible outcome. Several previous studies used spaceborne observations to analyze the atmospheric radiation budget and cloud characteristics in Antarctica. Scott and Lubin (2016) used CloudSat and Cloud-Aerosol Lidar and Infrared Pathfinder Satellite Observation (CALIPSO) observations and showed that Ross Island in Antarctica has the highest ice water content in clouds compared with Utqiaġvik, Alaska and Summit, Greenland, which leads to strong impacts on surface radiation energy fluxes. Listowski et al. (2019) used the DARDAR (raDAR/liDAR)-MASK cloud product in the southern polar regions and showed that liquid-containing cloud fraction is the highest over open ocean, followed by West Antarctica, and then the Antarctic Plateau. Scott et al. (2017) used satellite data to analyze cloud radiative effects over the WAIS, and found that longwave radiation from clouds dominates over shortwave reflection and absorption, resulting in a positive net cloud radiative effects at the surface with an annual mean value of 34 W m^{-2}. Using in situ observations from a tethered balloon, Lawson and Gettelman (2014) found supercooled liquid water existing in almost 50% of the observed clouds over Antarctica in the austral summer, and a modification of GCM to allow similar amount of supercooled liquid water as observed led to an increase of annual net cloud radiative effect over Antarctica by +7.4 W m^{-2}.

While there have been more ground-based observations of the high northern latitudes in regards to cloud properties, the Antarctic environment is distinct from the Arctic in a number of ways such as moisture and aerosol content (Abbatt et al., 2019; Liu et al., 2018; Shupe, 2011; Shupe et al., 2005, 2011; Silber et al., 2018; Silber, Verlinde, Cadeddu, et al., 2019). In Antarctica, extreme conditions such as very low temperatures, dry atmosphere, and katabatic winds are frequently seen (Bromwich et al., 2012). This is further compounded by the remoteness for operating and maintaining ground-based instruments, which results in a scarcity of observations to identify needed improvements in model parameterizations.

Previous evaluation on GCMs often focused on two cloud characteristics–cloud fraction and cloud thermodynamic phases (i.e., ice, liquid and mixed phases). By separating three cloud phases and their respective influences on atmospheric radiation budget, satellite observations illustrate a need to correctly simulate cloud cover and phase in all parts of the globe (Matus & L'Ecuyer, 2017). Several studies have previously used satellite data to evaluate cloud characteristics in various GCMs. Kay et al. (2012) found that CAM5

has global annual mean shortwave and longwave cloud forcing biases of −2 and −4 W m^{-2}, respectively, based on comparisons with the Clouds and the Earth's Radiant Energy System (CERES)–Energy Balanced and Filled (EBAF) data set. Cesana and Chepfer (2013) evaluated the LMDZ5B climate model against a spaceborne lidar–the CALIPSO. They found errors in cloud phase partitioning, as the model was unable to produce liquid clouds above 3 km. Another study from Bodas-Salcedo et al. (2019) showed that when implementing two new schemes (i.e., a mixed-phase cloud microphysics scheme and an aerosol-cloud interaction scheme) in the Hadley Center Global Environmental model (HadGEM3), both schemes dampen the negative cloud phase feedback of ice phase transitioning to liquid phase in a warmer climate, leading to a higher equilibrium climate sensitivity (ECS). Guo et al. (2020) used CALIPSO observations to evaluate the CAM5 model and found that the model underestimates (overestimates) global mean liquid (ice) cloud fraction at all altitudes. Li and Xu (2020) compared CloudSat and CALIPSO satellite observations with multiple GCMs and reanalysis data. Their study showed reduced low cloud cover with colder surface and stronger stability in the observations, yet not all of their model simulations were able to capture such feature. Besides satellite-based comparisons, other studies use aircraft observations to evaluate GCM simulations of high-latitude cloud characteristics. D'Alessandro et al. (2019) used aircraft-based in situ observations over the Southern Ocean around Punta Arenas, Chile and showed that CAM5 only simulates ice phase clouds below −15°C and underestimates ice water content in ice clouds by 1–1.5 orders of magnitude. Gettelman et al. (2020) used in situ observations around Hobart, Australia and found that the CAM6 simulations showed improvements by allowing supercooled liquid water to exist below −15°C compared with the older version CAM5. Differing from those previous studies, this work will focus on the Antarctic region, where GCMs are less frequently evaluated.

The United States (US) Department of Energy (DOE) Atmospheric Radiation Measurement (ARM) West Antarctic Radiation Experiment (AWARE) field campaign was deployed at McMurdo Station located on Ross Island, Antarctica, and provided unprecedented amount of comprehensive ground-based observations of Antarctic clouds. These observational data are valuable for the diagnosis of model biases and for providing observation-based constraints to future parameterizations in GCMs. This study focuses on the examination of cloud fraction and cloud phase from the AWARE campaign and the utilization of the AWARE data set to evaluate the National Center for Atmospheric Research (NCAR) Community Earth System Model version 2 (CESM2)/Community Atmosphere Model version 6 (CAM6) (Danabasoglu et al., 2020). This study is driven by two scientific questions: first, is CAM6 capable of simulating realistic representations of cloud fraction and phase? Second, are the biases of cloud fraction and cloud phase exhibited by the model related to thermodynamic biases that underly the formation of simulated clouds? In Section 2, the observational data set and model simulation are described in detail. Section 3 shows comparison results on a series of cloud characteristics and thermodynamic conditions. A discussion of the results and their implications are included in Section 4.

2. Observational and Simulation Data Set

2.1. Observations

The AWARE campaign provided a comprehensive data set of cloud and radiation observations during a full year in the Antarctic between December 2015 and December 2016 (Lubin et al., 2020). The campaign was based at the US McMurdo Research Station, located on Ross Island at 77°50′47″S, 166°40′6″E. During the sampling period, an ARM mobile facility (AMF) was deployed at the research station to measure atmospheric properties.

A cloud mask data set that quantifies cloud occurrence fraction and cloud phase was generated following Silber et al. (2018). This data set was largely based on measurements from two ground-based remote sensing instruments, namely the Ka-band ARM Zenith Radar (KAZR; Widener et al., 2012)—a millimeter wavelength zenith pointing radar capable of detecting fine cloud liquid and ice particles, and the High Spectral Resolution Lidar (HSRL; Eloranta, 2006)—a lidar capable of separating the backscattered signal of aerosols (e.g., hydrometeors) from the atmospheric molecular signal. The cloud masks provide four detection classes in each linearly interpolated 30 m by 10 s grid cell: clear sky (hydrometeor-free), ice phase-only hydrometeors, liquid phase (may also contain ice hydrometeors), and unknown phase. While from a volume-wise perspective the unknown phase mainly represents the ice phase class, these hydrometeors were detected

only with KAZR (above HSRL attenuation level), and hence, their phase cannot be reliably determined in bulk processing using only single-frequency zenith-pointing radar measurements (Silber et al., 2020). These cloud masks were quality controlled using microwave radiometer (MWR; Morris, 2006) measurements, which were used for liquid water path retrievals, and a ceilometer, which was used to detect cloud base height and delineate ice and liquid layers at the lowest altitudes. For temperatures $<-38°C$, all detected hydrometeors are defined as ice phase in the observations; for temperatures $>0°C$, all hydrometeors are defined as liquid phase. Between -38 and $0°C$, clouds can be ice, liquid or mixed phase.

Twice-daily at the research station (approximately 10 and 22 UTC), radiosondes were released to measure vertical profiles of temperature, water vapor partial pressure (e), winds, and pressure. Relative humidity with respect to liquid (RH_{liq}) and ice (RH_{ice}) are further derived from temperature and e measurements. These sounding data are used for analysis of thermodynamic conditions in conjunction with cloud retrievals. Relative humidity measurement uncertainty by ARM radiosonde is about 5%.

2.2. CAM6 Model Simulation

The NCAR CAM6 model, the atmospheric module of the CESM2 model, is compared against the observations. CAM6 utilizes the Morrison-Gettelman double-moment microphysics scheme (MG2), which simulates four classes of hydrometeors, namely liquid droplets, ice particles, snow, and rain (Gettelman et al., 2015; Gettelman & Morrison, 2015). MG2 allows for ice supersaturation and pre-existing ice in ice nucleation based on Shi et al. (2015), contains a heterogeneous ice nucleation parameterization (Hoose et al., 2010), and considers the contact angles of ice nucleating particles (INP) from Wang et al. (2014). MG2 cloud microphysics scheme is also coupled with Cloud Layers Unified by Binormals (CLUBB) scheme–a moist turbulence closure scheme developed by Larson et al. (2002) and Golaz et al. (2002a, 2002b) and implemented by Bogenschutz et al. (2013) into the CAM physics suite. CLUBB is involved in simulating boundary layer moist turbulence, stratiform clouds, and shallow convection, while deep convection is based on Zhang-McFarlane scheme by Neale et al. (2008) and G. J. Zhang and McFarlane (1995). Radiation is handled by the Rapid Radiative Transfer Model for General Circulation Models (RRTMG) (Iacono et al., 2000).

Temperature and horizontal wind fields in CAM6 simulation were nudged toward the NASA Modern-Era Retrospective analysis for Research and Applications version 2 (MERRA-2) (Molod et al., 2015), in order to represent closer-to-reality meteorological conditions seen at the study location. The nudging was done with a relaxation time of 24 h. Water vapor was not nudged, because it is part of the model tracer suite and state, which needs to be prognosed and consistent with the parameterizations in order to have any physical basis for the clouds. The nudging method was previously used in several studies that compared GCM simulations with observations (D'Alessandro et al., 2019; K. Zhang et al., 2014). The model setup is similar to Gettelman et al. (2020). The model was run using the default 32 sigma hybrid pressure layers from surface to 3 hPa at 30-min time steps, and a horizontal resolution of 0.5° latitude by 0.63° longitude. The analysis focuses on a single-column model output that is collocated with the McMurdo Station. The CAM simulation was spun-up for 6 months and run from June 1, 2015 until February 12, 2017. Only the dates that overlap with the AWARE campaign are used for comparison.

Variables used from CAM6 for comparison include ice water content (IWC, g/kg), liquid water content (LWC, g/kg), temperature (°C), water vapor mixing ratio (WVMR, g/kg), and cloud fraction (ranging from 0 to 1). WVMR was calculated for both the observations and the CAM6 output based on water vapor partial pressure (e) and atmospheric pressure (p): $WVMR = 0.622 \times e/(p-e)$. Combining e and saturation vapor pressure with respect to ice ($e_{s, ice}$) or liquid ($e_{s, liq}$), one can derive RH_{ice} and RH_{liq} for the simulation, respectively. The equations for $e_{s, ice}$ and $e_{s, liq}$ are based on Murphy and Koop (2005). RH_{ice} is only calculated for $T < 0°C$, and RH_{liq} is only calculated for $T > -38°C$. Three cloud phases are defined in the simulation based on thresholds of ice mass fraction defined in D'Alessandro et al. (2019). That is, liquid phase is defined as the ratio of IWC/cloud water content (CWC) < 0.1, ice phase is defined as IWC/CWC > 0.9, and mixed phase is defined as $0.1 \leq IWC/CWC \leq 0.9$. Here CWC is defined as the sum of IWC and LWC. A threshold of 10^{-4} was applied to model cloud fraction output as the limit of in-cloud condition. In addition, in-cloud condition in the simulation also needs to satisfy CWC $> 10^{-7}$ g m^{-3}, which is a typical limit used for defining in-cloud condensed water mass concentrations in GCMs (e.g., Patnaude et al., 2021).

All the analysis in this work is restricted to altitudes below 10 km. When comparing the model simulation output with radiosonde observations, even though sounding locations normally deviate from its original position after release, we found that all soundings are still within the same CAM6 model column as they reach 10 km. The model grid box used for comparison has surface altitude of 2.3 m, and the altitude of McMurdo Station is 69 m. In addition, we compared the selected model column at McMurdo Station with the surrounding columns and found relatively small differences in cloud characteristics among the adjacent model grid boxes (cf. Silber, Verlinde, Wang, et al., 2019, see their Figures S3–S5).

3. Results

3.1. Comparison of Times Series of Cloud Fraction, Cloud Phase and Thermodynamic Conditions

Time series of coincident observed and simulated cloud fraction and phase are shown in Figure 1. In this case, CAM6 overestimates cloud fraction between surface and 3 km from 12 UTC January 6 to 12 UTC January 8, 2016, and underestimates cloud fraction between surface and 3 km from 12 UTC January 8 to 00 UTC January 10, 2016 (Figures 1a and 1b). For cloud phase (Figures 1c and 1d), CAM6 simulates deeper layers of liquid and mixed phase (e.g., January 10–13) with a geometrical thickness of 1–3 km, while the observations often show geometrically thin layers of liquid phase with a thickness of 100–200 meters (e.g., from 12 UTC January 8 to 12 UTC January 9). In addition, the observed liquid phase layers are generally located on top of the clouds and above ice phase (precipitation), while the simulated liquid and mixed phase layers are located underneath the ice phase at the bottom of the cloud layer. This observed feature is consistent with a previous study, which showed that ice precipitation at cloud base occurs frequently (∼75%) over McMurdo (Silber et al., 2021). It is likely that the vertical resolution of the model may be too coarse to represent the gradients necessary to maintain various dynamical processes. For example, correctly simulating turbulent entrainment of newly produced ice nucleating particles (INPs) from above has been found to be important for cloud formation over the Southern Ocean (Atlas et al., 2020).

For the thermodynamic condition, a sounding profile of temperature and RH_{ice} at 1131 UTC is compared with a model output at 1130 UTC on January 10, 2016 (Figures 1e and 1f). The temperature biases are generally within 1–2°C, with the maximum cold bias of 4°C in the model at the cold point tropopause at 9 km (Figure 1e). Compared with the RH sounding data (Figure 1f), the simulation shows high RH_{ice} biases of 20%–30% above 3 km, and low RH_{ice} biases of 10%–20% between 1.5 and 3 km. These differences in RH_{ice} are consistent with the fact that cloud fraction below unity was observed above 3 km (Figure 1a) while the simulated cloud fraction is close to unity (Figure 1b). The sharp decrease of RH in CAM6 around 1–2 km is also consistent with the narrow hydrometeor-free layer simulated at that time and location. Both temperature and RH sounding data are gridded onto the coarser CAM6 vertical bins, yet sharp changes in observed RH (e.g., at 5 km) are still not captured by the simulation.

Model biases of RH_{ice} and cloud fraction (henceforth, dRH_{ice} and dCF, respectively) are defined here as the simulated values minus the observed values. The histograms of their absolute values, $|dRH_{ice}|$ and $|dCF|$, are shown in Figure 2 for the duration of the entire AWARE campaign. Most $|dRH_{ice}|$ values are less than 20%. $|dCF|$ has a bimodal distribution with the primary and second peak near 0 and 1, respectively. The bin of $|dCF| < 0.05$ becomes the secondary peak after excluding cases when both observations and simulations show CF = 0 as well as when they both show CF > 0.95. The peak at $|dCF| < 0.05$ suggests that CAM6 output captures the observed cloud fraction. The peak of $|dCF|$ near 1 indicates that model either completely misses the observed cloud fraction or produces spurious cloud fraction at one.

3.2. Seasonal Variabilities of Cloud Fraction, Temperature, Water Vapor and RH_{ice}

A comparison on average cloud fraction for the entire campaign as well as four seasons of a year is conducted (Figure 3a). For all the vertical profile comparisons in this section, observations are gridded into the model vertical levels. Average cloud fraction of the observations is calculated as the number of in-clouds samples divided by the total number of samples at 10-s resolution in a certain time period. Average cloud fraction biases are calculated as the simulated minus the observed seasonal or annual average cloud fractions. Average cloud fraction and average cloud fraction biases exhibit both seasonal and altitudinal dependence. Observed
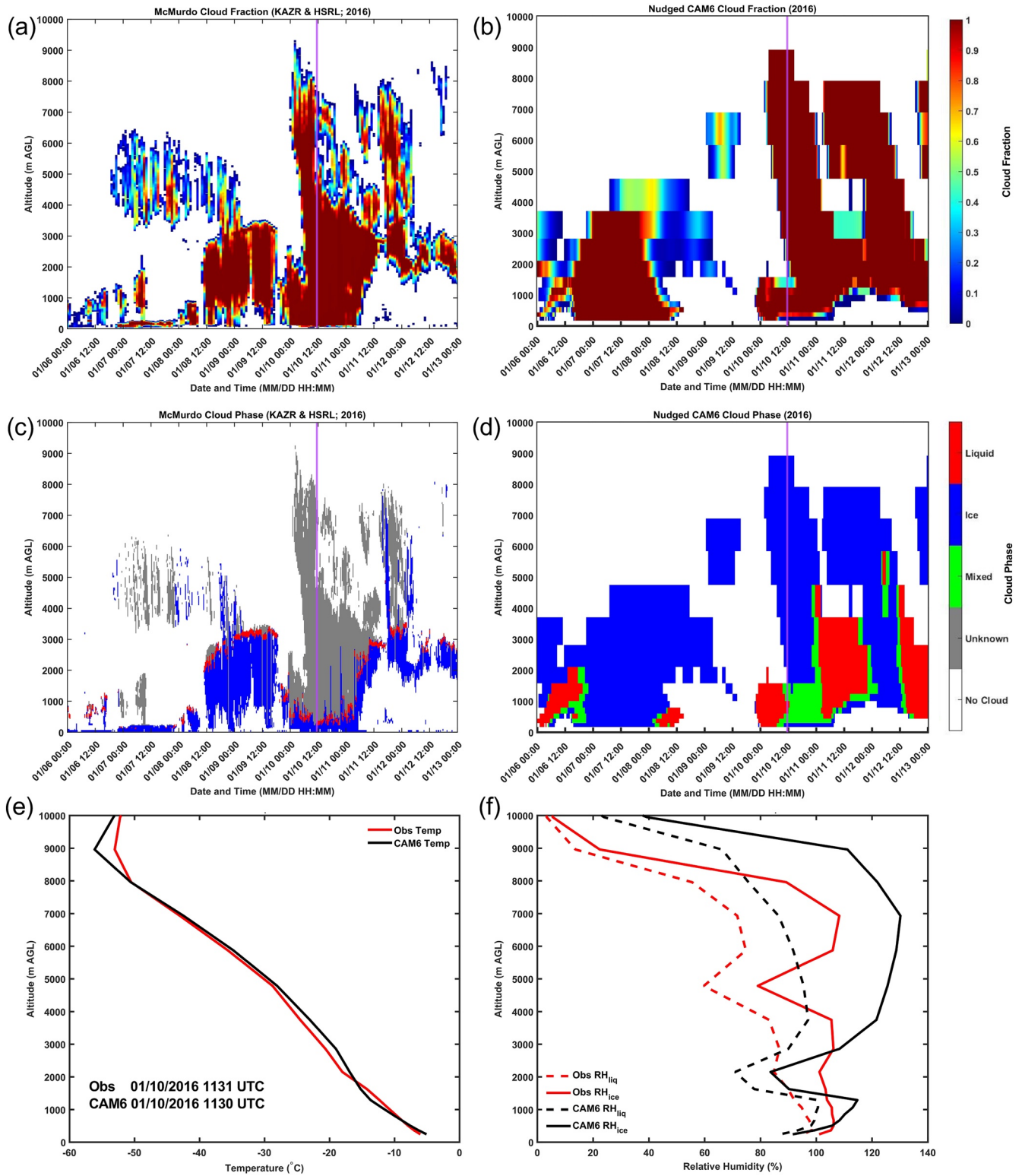
Figure 1. Simultaneous times series based on the ARM West Antarctic Radiation Experiment campaign observations and CAM6 simulation between 00 UTC on January 6, 2016 and 00 UTC on January 13, 2016. (a) Cloud fraction calculated for every hour based on ground-based observations. (b) CAM6 cloud fraction. (c) Cloud phases in four types based on ground-based observations at 10-s resolution. (d) CAM6 cloud phase. (e) Temperature profile based on radiosonde released at 1131 UTC on January 10, 2016 re-gridded to model altitudes, compared with model output at 1130 UTC on January 10, 2016. (f) As in (e) but showing the RH_{ice} and RH_{liq} profiles. Purple vertical lines in curtain plots denote sounding release time.
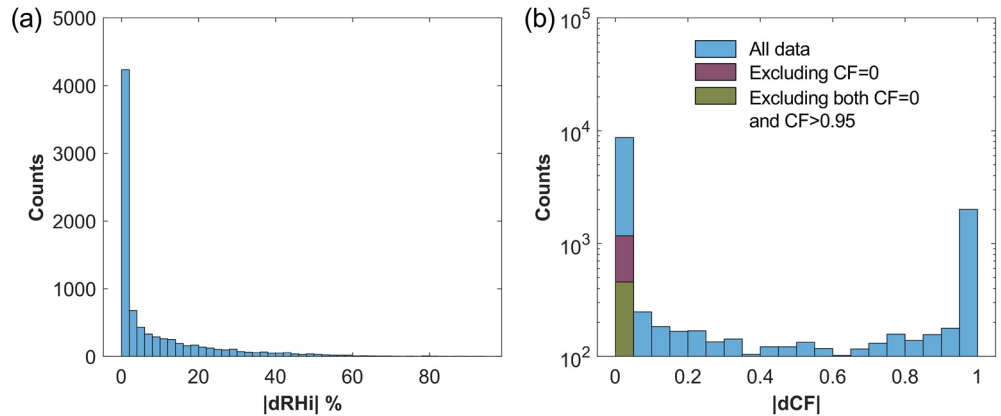
Figure 2. Histograms of (a) |dRH$_{ice}$| and (b) |dCF| occurrences during the entire West Antarctic Radiation Experiment campaign. Note the logarithmic *y*-axis scale in panel (b). Red bar is similar to blue bar in the first bin but excludes cases when both observations and simulations show CF = 0. Green bar further excludes cases when both observations and simulations show CF = 0 and when they both show CF > 0.95.

cloud fraction exhibits the maximum at approximately 1 km. The austral fall (March, April, May; MAM) and austral summer (December, January, February; DJF) show the highest cloud fraction below and above 1.5 km, respectively. The austral spring (September, October, November; SON) and austral fall (MAM) show the smallest cloud fraction below and above 3 km, respectively.

CAM6 exhibits much lower cloud fractions below 2 km, and its maximum average cloud fraction occurs at a slightly higher altitude, that is, approximately 2 km for austral summer and fall and 5.5 km for austral winter (June, July, August; JJA) and spring. In addition, the observed cloud fraction decreases significantly with altitudes and becomes less than 0.2 above 4 km. In comparison, simulated cloud fraction remains above 0.2 up to 7.5 km and decreases significantly above that altitude. Accordingly, a change in the sign of cloud fraction biases is seen around an altitude of 2–3 km. That is, negative and positive cloud fraction biases are seen for each seasonal averaging period below and above this altitude, respectively (Figure 3b).

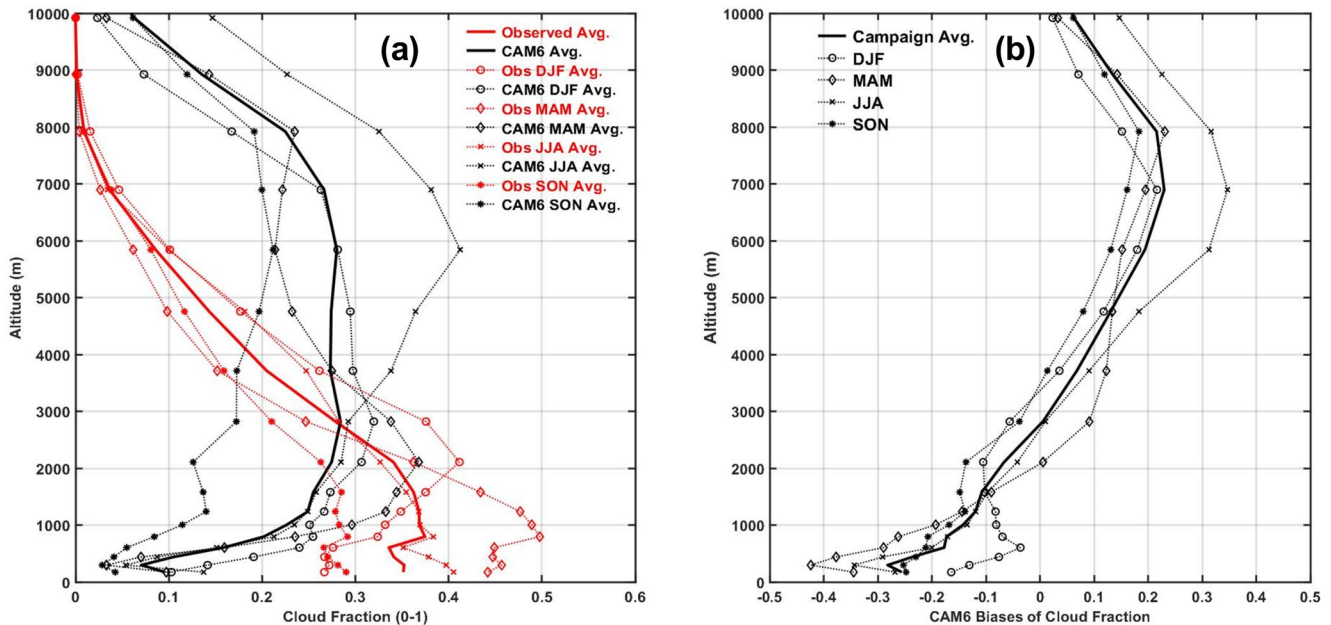**Figure 3.** (a) Vertical profiles of average cloud fraction based on observations and model simulation for different seasons (i.e., December, January, February, March, April, May, June, July, August, and September, October, November) as well as for the entire West Antarctic Radiation Experiment campaign. (b) Cloud fraction biases (model minus observation) averaged by each season and the entire campaign.
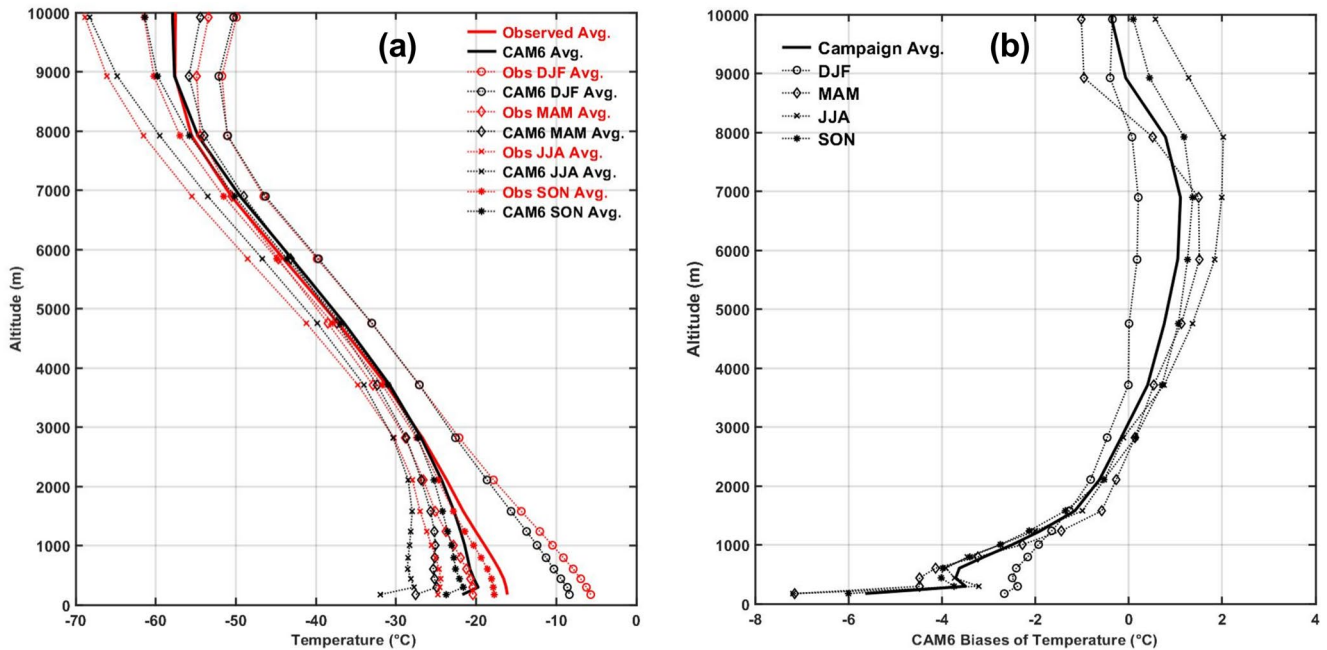
Figure 4. Similar to Figure 3, but for temperature.

Below 1 km, MAM shows the largest negative cloud fraction bias with the peak bias of −0.42 at 0.25 km, and DJF shows the smallest negative bias (around −0.2 to −0.1). Above 3 km, CAM6 exhibits the largest positive cloud fraction bias during austral winter (JJA), with the maximum value of 0.35 at 6.5 km.

Average temperature and temperature biases are shown in Figure 4. Since the model was nudged toward re-analysis data for temperature, thus temperature biases shown here originate from biases in reanalysis data. Negative (positive) temperature biases are seen below 2 km (between 2 and 8 km) in all averaging periods (Figure 4b). The magnitudes of the negative temperature biases decrease from −6 to 0°C with increasing altitude at 0–2 km, while the magnitudes of the positive biases increase from 0 to 2°C with increasing altitude at 2–8 km. Seasonal variabilities in temperature biases are relatively small, aside from the DJF averaging period, which has the smallest magnitudes of both negative and positive biases. Near-surface temperature inversions are seen in observations during austral fall and winter (MAM and JJA) at 0.25 km with an average magnitude of about 1°C, while the simulation shows more pronounced near-surface temperature inversions (~5°C on average) than observations for all seasons except DJF (Figure 4a).

Similar to the near-surface temperature inversions, small near-surface moisture inversions were observed at 0.25 km during austral fall and winter (MAM and JJA), while the simulation shows much stronger moisture inversions at higher altitude, with average WVMR magnitudes of 0.1–0.2 g/kg inside deeper inversion layers that extend from 0.25 to 1 km (Figure 5a). In addition, more surface moisture was observed during the austral summer. The simulation can represent the higher moisture during austral summer. Below 2 km, CAM6 exhibits negative WVMR biases in all seasons except DJF (Figure 5b). Above 2 km, the model exhibits positive WVRM biases in all seasons. Similar to the seasonality of temperature biases, the WVMR biases in DJF differ the most from the rest of the year. While the temperature biases of DJF are the smallest for all altitudes, the water vapor biases of DJF are smallest in magnitude below 1 km and largest above 1 km.

The seasonal averages of RH_{ice} as well as RH_{ice} biases are shown in Figure 6. Observation profiles show that RH_{ice} has a local minimum (60%–70%) close to the surface at about 0.5 km (Figure 6a). The maximum RH_{ice} occurs at 1.5 km (70%–80%), and above this altitude the observed RH_{ice} decreases monotonically from 60%–80% to 10%–40% at 10 km. CAM6 shows similar RH_{ice} variability with altitudes, but with a smaller local minimum RH_{ice} of 50%–70% at 0.25 km, and a larger maximum RH_{ice} of 70%–90% at 1.5 km. CAM6 also consistently shows higher RH_{ice} than observations above 1 km. Thus, CAM6
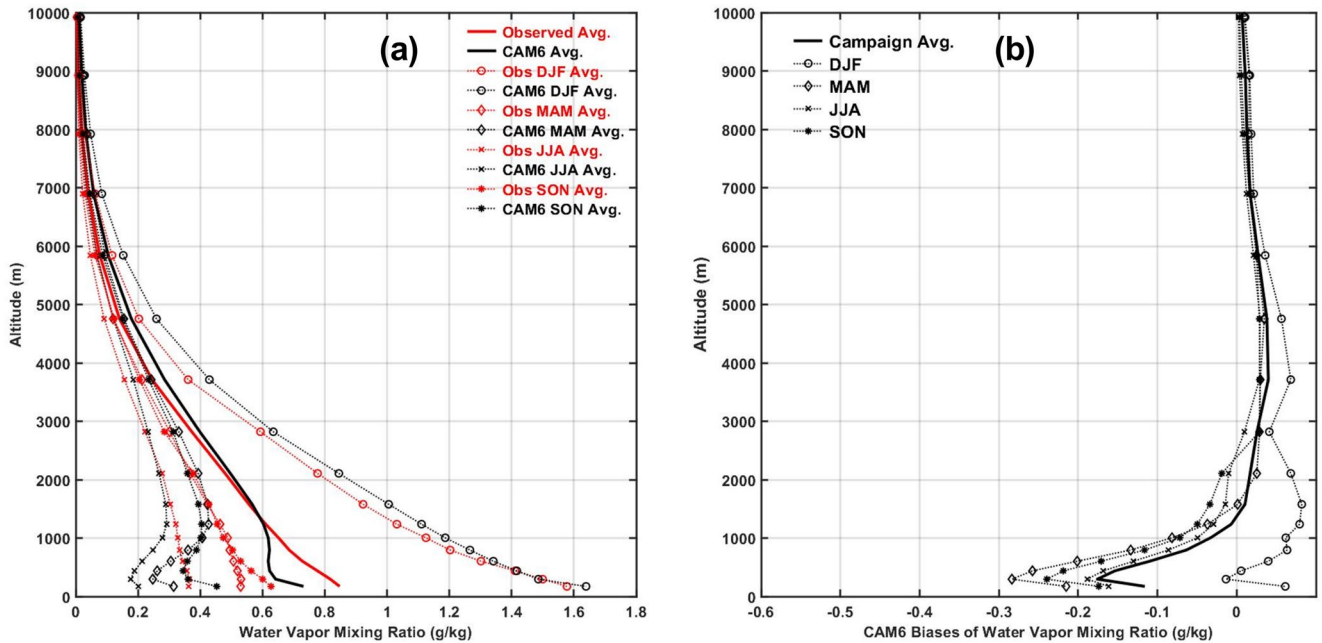
Figure 5. Similar to Figure 3, but for water vapor mass mixing ratio.

exhibits positive biases between 1 and 10 km, negative RH_{ice} biases between 0.1 and 1 km, and positive biases at the lowest 0.1 km (Figure 6b).

A comparison among MERRA-2, CAM6 and observations is shown for temperature, WVMR and RH_{ice} (Figure 7). The comparison results show similar magnitude and sign of temperature biases for CAM6 and MERRA-2. CAM6 shows slightly larger temperature biases below 1.5 km compared with MERRA-2, indicating that nudging contributes to some but not all of the temperature biases shown in the model. WVMR in CAM6 shows smaller low bias below 1 km and larger high bias above 4 km compared with MERRA-2,
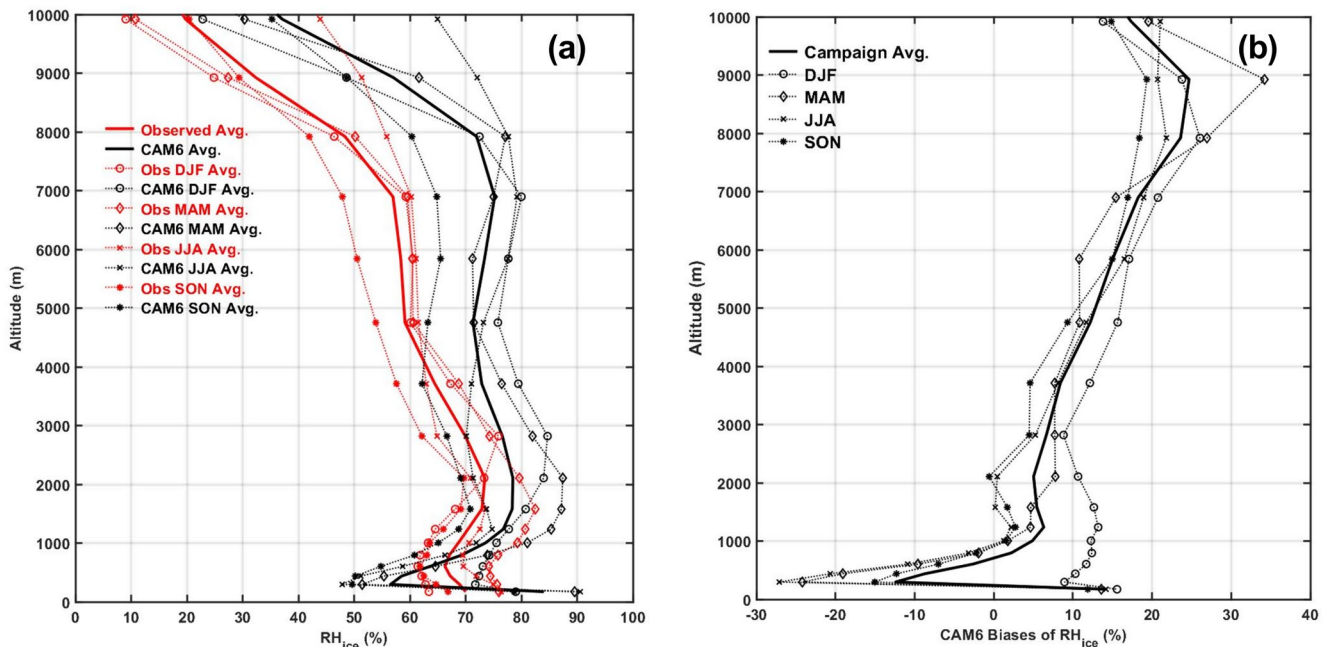

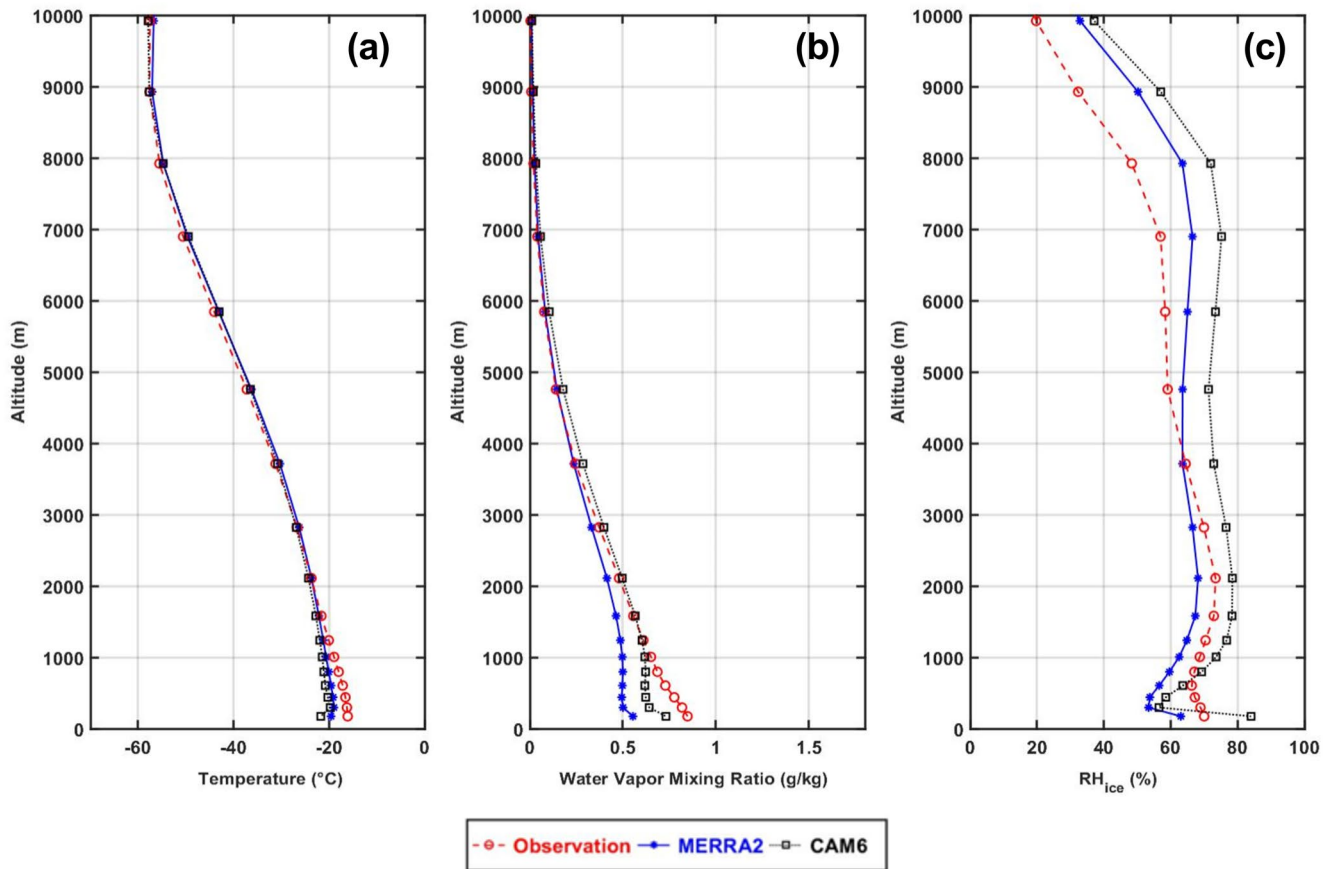**Figure 6.** Similar to Figure 3, but for RH_{ice}.

Figure 7. A comparison among Modern-Era Retrospective analysis for Research and Applications version 2, CAM6 and observations at McMurdo Station over the time period of the West Antarctic Radiation Experiment campaign is shown for (a) temperature, (b) water vapor mixing ratio and (c) RH_{ice}.

which also leads to a smaller low bias of RH_{ice} below 1 km and a larger high bias of RH_{ice} above 4 km in CAM6 than MERRA-2.

3.3. Evaluation of Cloud Phase and Related Thermodynamic Conditions

Distributions of various cloud phases are shown for observations and simulations in Figure 8. Figure 8 sums up the total ground-based observation samples at 10-s resolution as well as the closest model grid matching with each observation sample in various conditions (i.e., various cloud phases and clear-sky conditions). This method provides a total of 3.4 million samples in each of the 334 vertical layers for the 10-s observations from surface to 10 km. For total in-cloud frequency, CAM6 underestimates and overestimates total cloud frequency below and above 2.5 km, respectively, which is consistent with the cloud fraction biases seen in Figure 3. For these collocated observation and model data, CAM6 underestimates ice phase occurrences below 2.5 km and overestimates ice phase above 2.5 km. For the unknown phase in the observations, if we assume that all unknown phase in the observation was liquid-containing clouds at 0.3–2 km, the model would still overestimate liquid-containing cloud phase occurrences at those levels. However, above 2 km, if we assume that all unknown phase was liquid-containing clouds, the model would underestimate the liquid-containing cloud phase occurrences. Since liquid phase is less likely to occur at higher altitudes because of the lower temperatures (e.g., McErlich et al., 2021), it is more likely that the model also overestimates liquid occurrence at higher altitudes.

Figure 9 provides a more detailed evaluation of the simulated cloud phase by comparing each type of observed cloud phase with the closest model output in time. Observations are separated into four types of conditions–ice phase, liquid phase, unknown phase, and clear-sky condition. When observations show ice
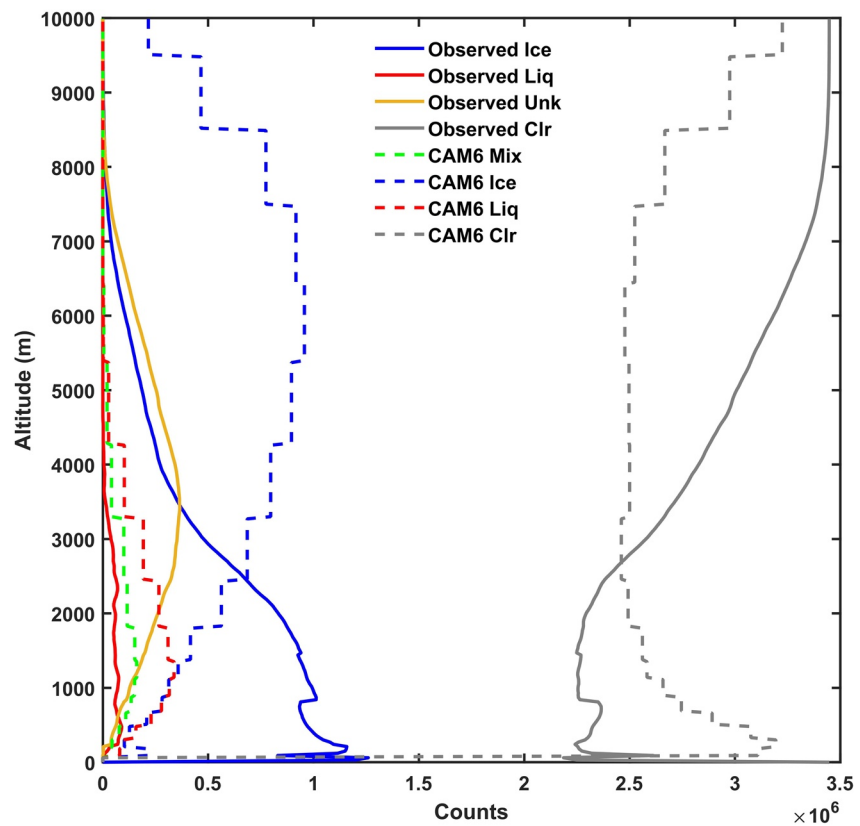
Figure 8. Observed (solid lines) and simulated (dashed lines) cloud phases, shown in number of samples for the entire campaign. Clear-sky samples are shown in gray color. Cloud phases are based on observations at 10-s resolution, which include ice, liquid, and unknown phases. They are compared with the closest model output in time.

phase, the dominant cloud phase in the collocated simulation output is also ice phase, although the simulation only captures about 30%–50% of the observed ice phase below 4 km and misidentifies the majority of the ice phase below 2 km as clear-sky conditions. When observations show liquid phase, the simulation captures about 20% of them as liquid phase and 10% as mixed phase, while misidentifies 20% of them as ice phase and the rest as clear-sky conditions. When observations show unknown phase, the simulation captures 50%–90% of these instances as ice phase, in agreement with the previous finding that unknown phase is most likely ice phase (Silber et al., 2020). For the observed clear-sky conditions, the simulation correctly represents about 60%–80% of these instances, while the rest is mostly misidentified as ice phase. Overall, these comparisons show that the dominant phase of simulation matches well with the observed phase under each condition especially when combining simulated liquid and mixed phase occurrences to compare with observed liquid phase, although the simulation only captures 30%–50% of the observed ice and liquid phase.

Occurrence frequencies of ice, liquid, and mixed phases normalized by total in-cloud samples are depicted in Figure 10. Figure 10 examines the correlation between cloud phase biases and cloud fraction biases, and also redefines observed cloud phases on a coarser scale. Differing from Figures 8 and 9 that use cloud phases defined by high-resolution (10-s) observations, the analysis in Figure 10 defines observed cloud phase by calculating the proportion of ice phase among all cloud phases within ± 15 min surrounding each half-hourly model output. Note that this proportion (or relative frequency) of ice phase is not the same as ice cloud fraction, since the former value equals the number of ice phase divided by the number of in-cloud samples, while the latter value equals the number of ice phase divided by the number of total samples (i.e., both in-cloud and clear-sky conditions). Observation samples with ice phase proportion <0.1, between 0.1–0.9 and > 0.9 are defined here as liquid, mixed and ice phase, respectively.
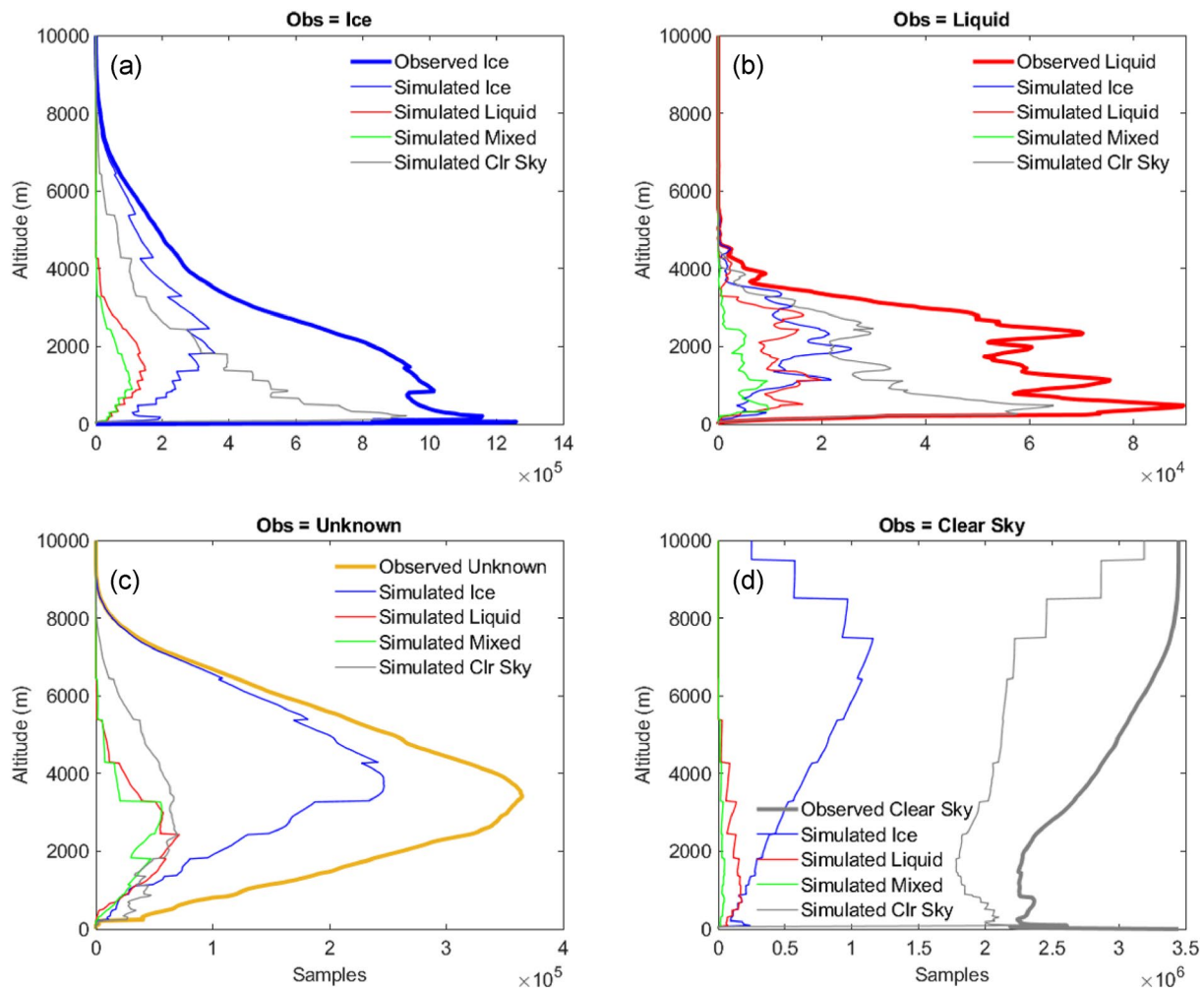
Figure 9. Comparisons of observed and simulated cloud phase when observations show (a) ice phase, (b) liquid phase, (c) unknown phase, and (d) clear-sky condition. The number of observed samples is shown in thick lines, while the simulation output is designated by thin lines. Cloud phases are based on 10-s resolution observations. The model output closest to each observation sample is used for this comparison.

The occurrence frequency of each cloud phase is normalized by the total number of cloud occurrences in a certain range of cloud fraction. The unknown phase in the observations between −38°C and 0°C is excluded from these calculations. Differences in cloud phase frequencies are seen depending on the cloud fraction ranges. Overall, at cloud fraction >0.9, the simulation underestimates (overestimates) ice (liquid) phase frequency, particularly below 3 km by 20%–50% points. As cloud fraction decreases, the simulation shows smaller biases in ice and liquid phase frequencies below 2 km, but shows larger biases in ice and mixed phase frequencies between 2 and 5 km, that is, overestimating (underestimating) ice (mixed) phase frequency by up to 30% points. For observations below 5 km, ice (mixed) phase frequency increases (decreases) with cloud fraction, while liquid phase frequency is relatively independent of cloud fraction. Comparatively, simulation shows opposite trend below 5 km, that is, simulated ice (liquid) phase frequency decreases (increases) with cloud fraction, while mixed phase frequency slightly increases with cloud fraction. Above 5 km, both observations and simulation show nearly 100% of ice phase.

To examine the sensitivity of the comparison results to the unknown phase, Figures S1–S3 assume the observed unknown phase at −38–0°C being ice, liquid and mixed phase, respectively. For cloud phase frequencies of the entire cloud fraction range, including the observed unknown phase in ice phase leads to a slightly larger low-level bias of ice phase in the simulation compared with Figure 10. Including the observed unknown phase as either liquid or mixed phase leads to significant increases of the frequencies of these phases, since the number of samples for these phases is originally small in Figure 10. Such results agree
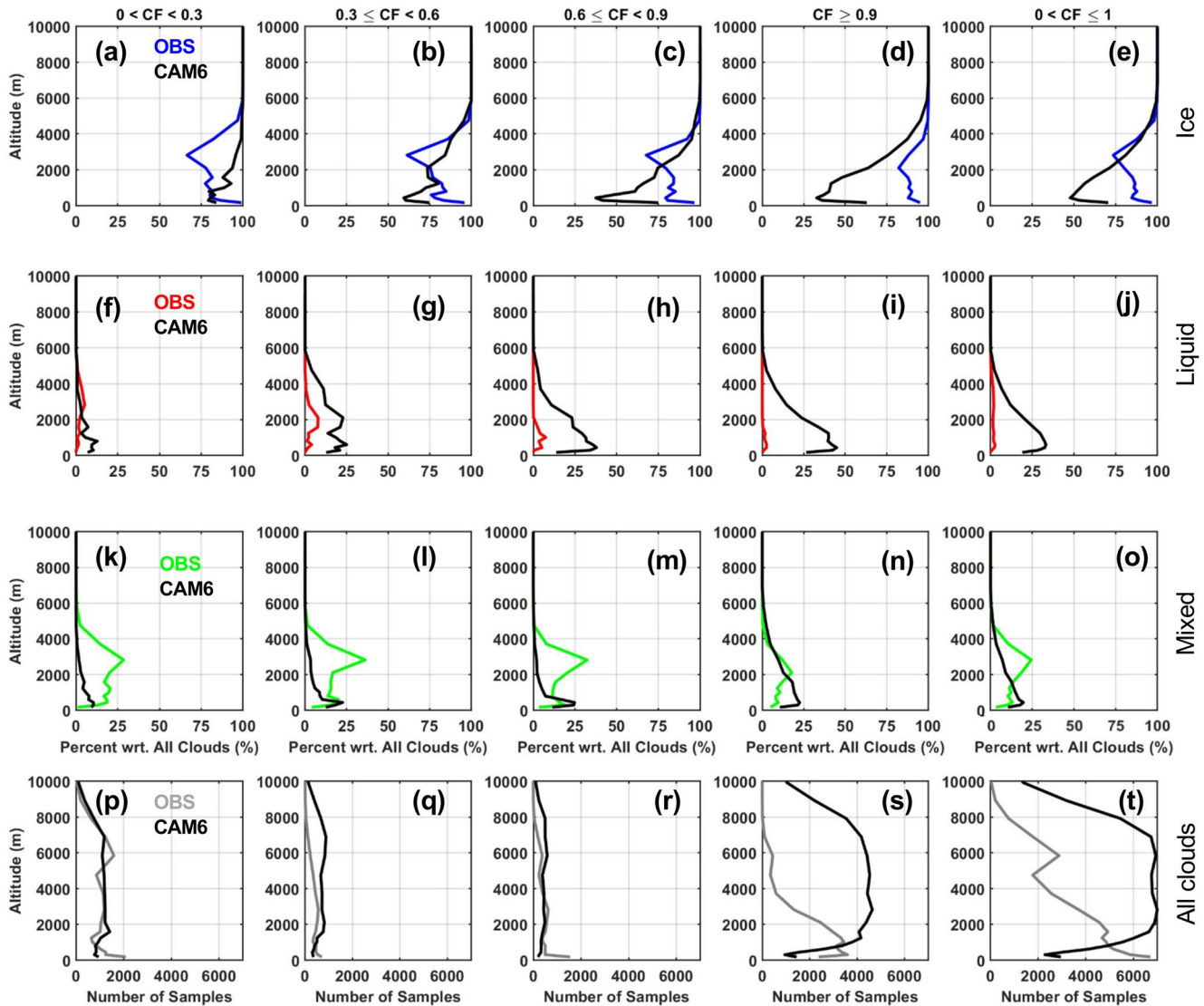
Figure 10. Comparisons of cloud phase frequency between observations and the model simulation, including (a–e) ice phase, (f–j) liquid phase, and (k–o) mixed phase. The last row (p–t) stands for the number of total in-cloud samples for various cloud fraction ranges. Each cloud phase is separated into five ranges of cloud fraction (in five columns) and is compared for the entire AWARE campaign. 10-s resolution observation data are averaged to 30 min surrounding the closest model output to derive three cloud phases in this figure. The observed unknown phase below −38°C and above 0°C is included as ice and liquid phase, respectively. The remaining unknown phase between −38 and 0°C is excluded.

with the volume-wise dominance of ice in the unknown class (e.g., Figure 1), and also insinuate on a greater relative occurrence of liquid or mixed-phase determined as unknown at lower-levels. Note that this comparison in Figure 10 analyzes the occurrence frequencies of various cloud phases for the entire observation and simulation data set(s) without restricting the observations to be compared against the closest model output only, which differs from the comparisons of concurrent observations and model output in Figures 8 and 9.

3.4. Impacts of Thermodynamic Conditions on Cloud Phase and Fraction Biases

As both cloud fraction and cloud phase are governed by the thermodynamic conditions, the correlations of model biases of cloud fraction and cloud phase with respect to biases of RH_{ice} are further examined. Figures 11a–11d depict the number of samples for correctly simulated ice and liquid phase (hits) and incorrectly simulated ice and liquid phase (misses) binned by the absolute RH_{ice} biases ($|dRH_{ice}|$) of 0%–5%, 5%–20%, >20%, and all $|dRH_{ice}|$. The comparison is conducted by comparing each observation sample with the closest

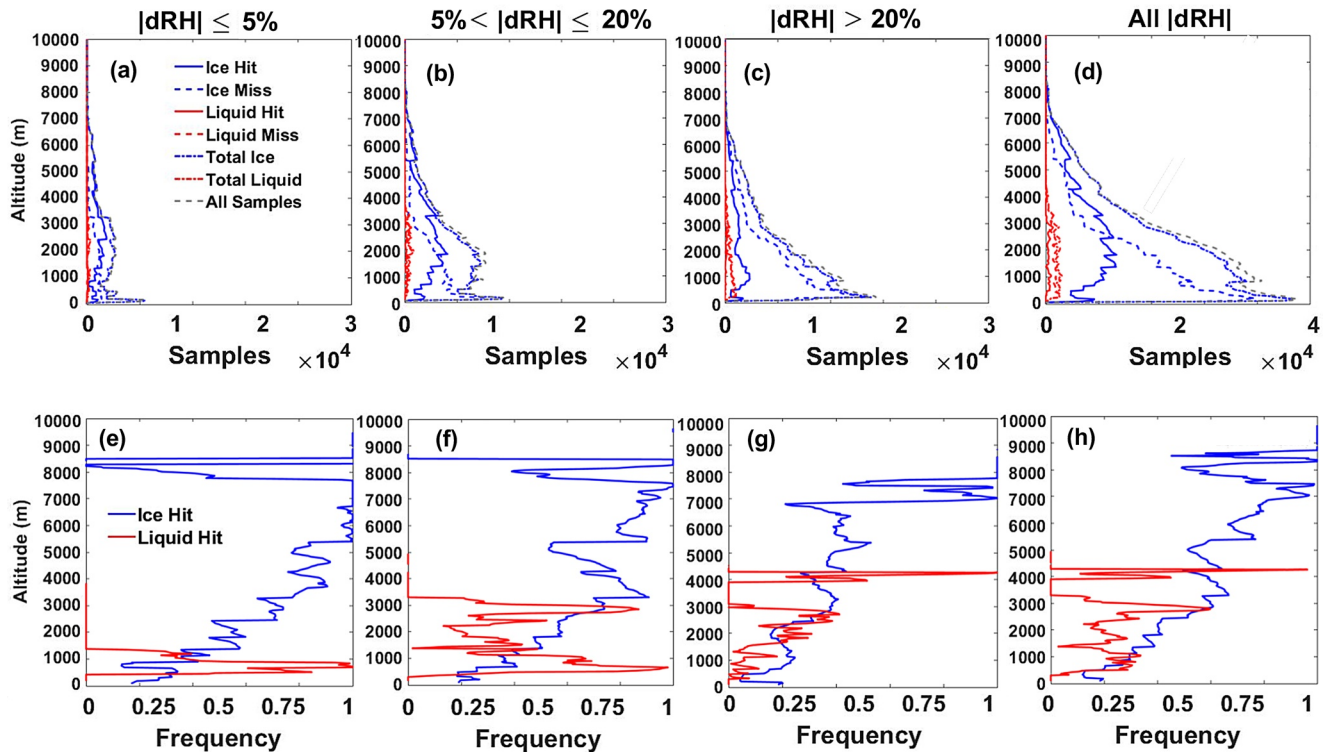**Figure 11.** Hits and misses of ice and liquid phase in terms of (a–d) number of samples and (e–h) frequencies, binned by $|dRH_{ice}|$ biases, including $|dRH_{ice}| \leq 5\%$, $5\% < |dRH_{ice}| \leq 20\%$, $|dRH_{ice}| > 20\%$, and all $|dRH_{ice}|$. Each observation sample is compared with the closest model output. The gray dashed line denotes all samples used for the comparison within a certain $|dRH_{ice}|$ range. The observed unknown phase is excluded from this analysis.

model output in time, similar to Figure 9, but shows fewer samples than Figure 9. This is because Figure 11 only uses the model output within ± 30 min of the radiosonde RH measurements to calculate $|dRH_{ice}|$, which also reduces the number of model output used for cloud phase comparisons. Figures 11e–11h show the occurrence frequencies of ice (or liquid) phase hits and misses, normalized by the total number of samples when observations show ice (or liquid) phase. For ice phase comparisons, when $|dRH_{ice}| \leq 5\%$, most (>95%) of the observed ice phase is captured by the model between 5.5 and 7.5 km, while the frequencies of capturing ice phase decrease from 90% to 20% with decreasing altitudes from 5.5 km to surface. This result indicates that the model has more difficulties of capturing lower-level ice phase than higher-level ones. A decreasing trend is seen in the frequencies of model capturing ice phase when larger absolute RH biases are seen. These results suggest that larger magnitudes of absolute RH_{ice} biases likely cause higher frequencies of model misrepresenting ice phase. For liquid phase, due to the small sample size, the frequency of hits of liquid phase is more variable and the overall frequency of capturing liquid phase correctly is lower than 0.7. For lower-level liquid phase below 1.5 km, simulation samples with smaller absolute $|dRH_{ice}|$ show high frequencies of capturing liquid phase as observed. The results suggest that absolute RH_{ice} bias plays an important role in the success of CAM6 simulating cloud phase accurately.

To isolate the influences of thermodynamic conditions on cloud fraction, correlations of model biases of cloud fraction (dCF) with respect to biases of RH_{ice} and RH_{liq} (i.e., dRH_{ice} and dRH_{liq}, respectively) are analyzed (Figure 12). Positive relationships are seen between cloud fraction and RH biases. Two types of linear regressions are calculated, one with all points of dCF included (Figures 12a and 12c) and the other one focusing on the less dominant dCF values by excluding dCF values of −1, 0, and 1 (Figures 12b and 12d). The latter type of linear regression examines the correlation between dRH and dCF when the simulation produces partially correct cloud fraction values instead of completely correct (dCF = 0) or completely wrong (dCF = +1 or −1) values. Slightly higher coefficients of determination (r^2) are seen in the latter linear regressions (0.294, 0.303) compared with the former regressions (0.257, 0.268). In addition, slightly higher positive slopes are seen when removing dCF of 0 and ± 1. For dRH_{ice}, removing dCF of −1, 0 and 1 shows
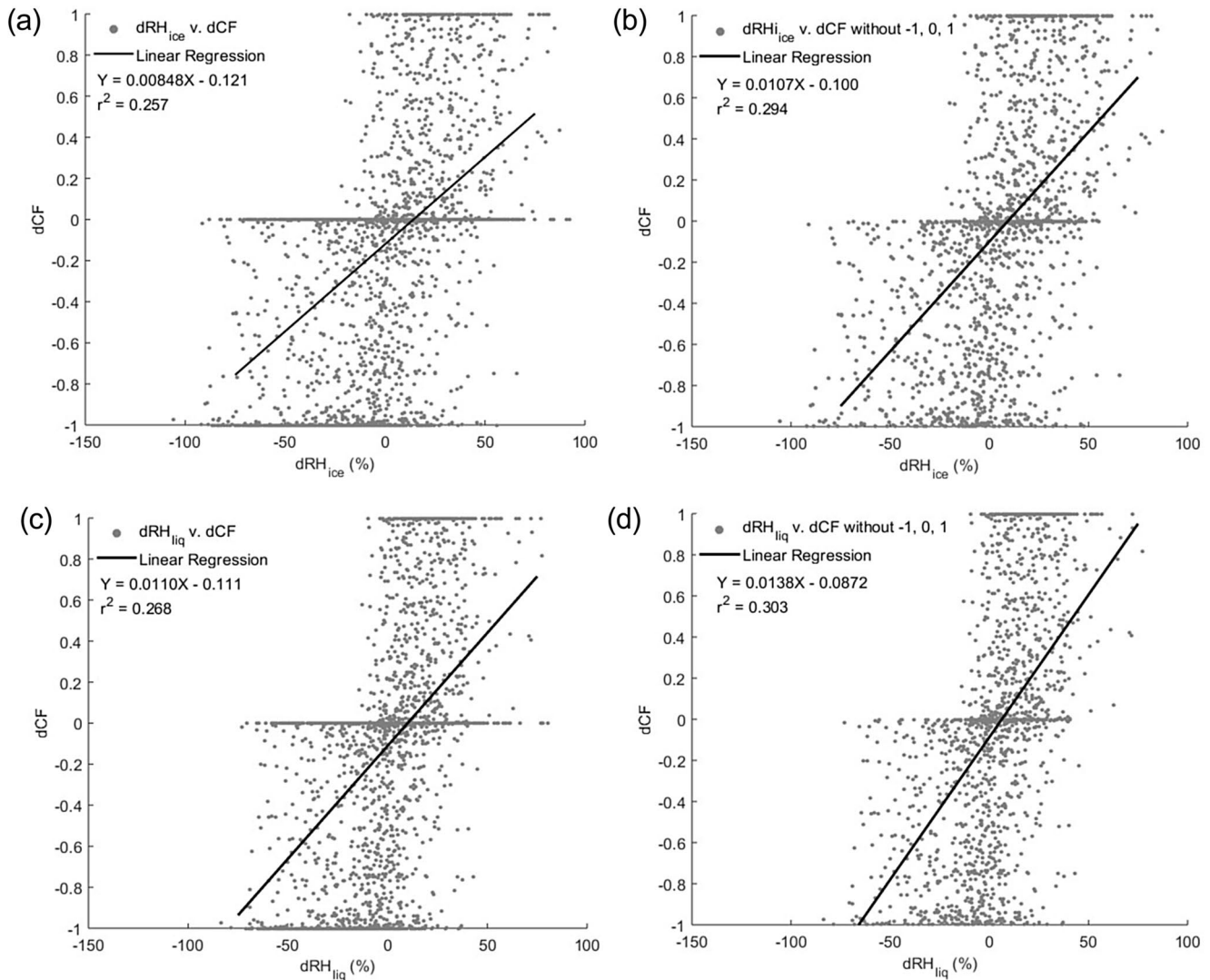
Figure 12. Correlations of dCF with respect to (a and b) dRH_{ice} and (c and d) dRH_{liq}. Linear regression is applied to all data in (a) and (c), while (b) and (d) excludes dCF = −1, 0, and 1.

$dCF = 0.0107 \times dRH_{ice} - 0.100$, while using all dCF values shows $dCF = 0.00848 \times dRH_{ice} - 0.121$. Similarly, the linear regression with respect to dRH_{liq} shows $dCF = 0.0138 \times dRH_{ice} - 0.0872$ when excluding dCF = −1, 0, and 1, and $dCF = 0.0110 \times dRH_{ice} - 0.111$ when using all data. Slightly lower correlations are seen when including cases of dCF = −1, 0, and 1, likely because dRH values show larger variations when either one or both of the data set(s) show clear-sky conditions. That is, when either observation or simulation is clear sky while the other one is in-cloud (i.e., dCF = 1 or −1), or when both observation and simulation are clear sky (i.e., part of the cases of dCF = 0), the data set(s) with clear-sky conditions can have RH ranging from a few percentage points to near saturation, while the data set with in-cloud conditions often has RH around saturation, therefore leading to a wide range of dRH values.

The correlations of cloud fraction biases with respect to RH biases demonstrate the importance of further understanding key factors contributing to RH biases. Thus, we decompose the biases of RH into three components, that is, contributions of temperature biases (dRH_T, Figures 13a and 13d), contributions of water vapor biases (dRH_q, Figures 13b and 13e) and an higher order term representing their covariance biases ($dRH_{q,T}$, Figures 13c and 13f). This method is similar to that previously described in Diao et al. (2014). $dRH_{ice,T}$ has both a weaker contribution (slope = 0.0530) and weaker correlation ($r^2 = 0.014$) with respect to dRH_{ice} than $dRH_{ice,q}$ (slope = 0.976; $r^2 = 0.71$). Similarly, water vapor biases are the main contributor to
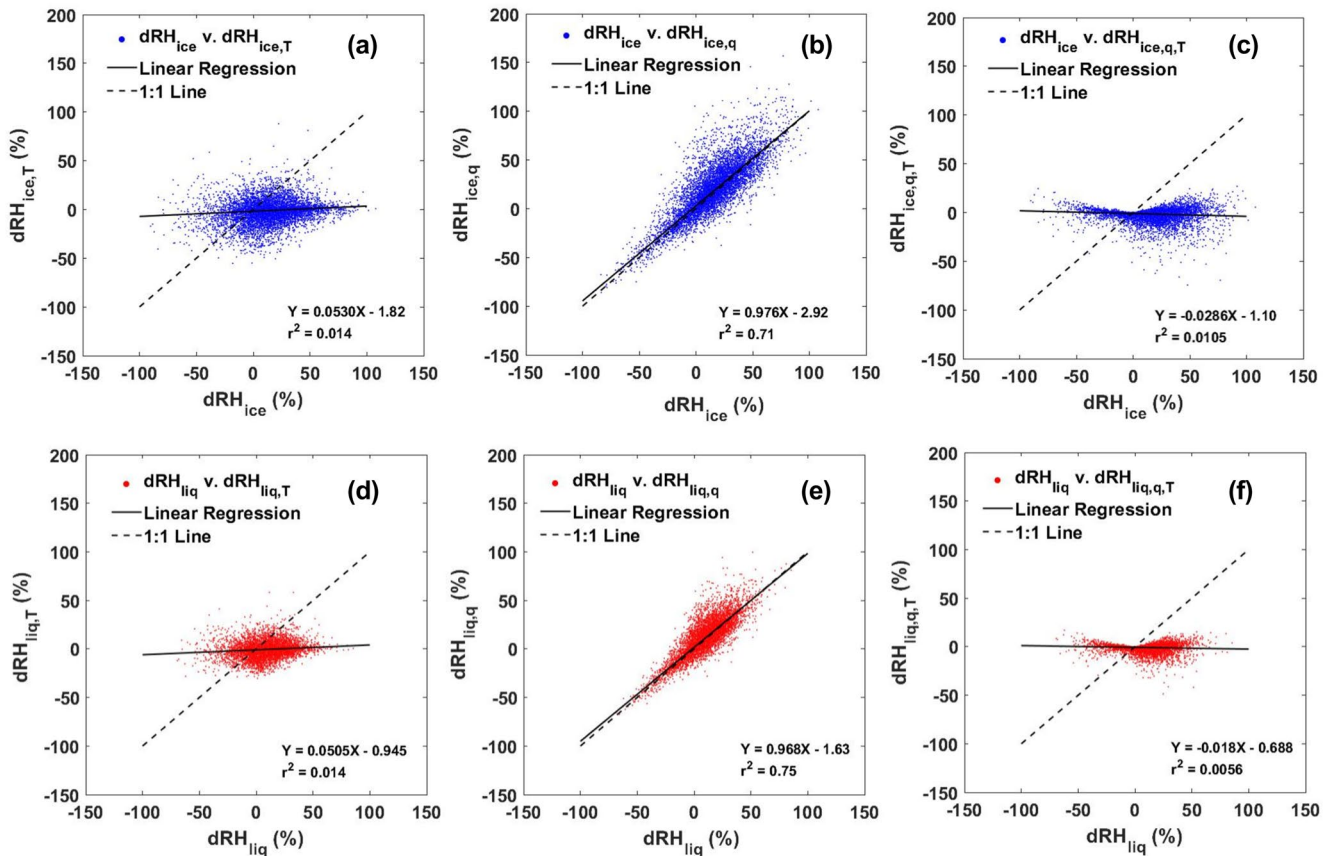
Figure 13. Decomposition of (a)–(c) dRH_{ice} and (d)–(f) dRH_{liq} into three components, that is, (a) $dRH_{ice,T}$, (b) $dRH_{ice,q}$, (c) $dRH_{ice,q,T}$, and (d) $dRH_{liq,T}$, (e) $dRH_{liq,q}$, (f) $dRH_{liq,q,T}$. Linear regression is applied to each sub-plot.

dRH_{liq} biases. Thus, water vapor biases have a much stronger influence on both RH_{ice} and RH_{liq} biases than temperature biases. Combining this finding with the results from Figures 11 and 12, it indicates that the model biases of cloud phase and cloud fraction are correlated and possibly attributable to misrepresentations of water vapor concentrations in CAM6.

4. Discussion and Summary

One of the AWARE campaign's main goals is to better understand the processes that affect changes in Antarctica, which is heavily influenced by the atmospheric phenomena present in the local region. This study identifies biases of cloud characteristics in CAM6 at the McMurdo research location and specifies concurrent biases exhibited in cloud fraction, cloud phase and thermodynamic conditions (i.e., temperature, RH, and WVMR). Methods are developed to compare higher-resolution radar-lidar cloud mask data and collocated radiosonde profiles of temperature and moisture with a coarser-scale simulation by CAM6. By doing so, model biases in cloud fraction, cloud phase, temperature, RH and WVMR are quantified both seasonally and during the entire campaign. Furthermore, correlation analyses suggest thermodynamic conditions, particularly atmospheric moisture, play a key role in determining the model biases of cloud characteristics. Even though the bulk Antarctic cloud properties observed over McMurdo may not fully represent statistics of Antarctic clouds at a larger synoptic scale (Silber, Verlinde, Cadeddu, et al., 2019), the station served as the only location equipped with required infrastructure to support such a comprehensive deployment, and still allows the examination of important cloud-related processes and the atmospheric state. In addition, cloud formation at McMurdo Station is affected by the local small-scale complex terrain, wind regime, and mesoscale activity such as cyclogenesis around Ross Ice Shelf and Ross Island in particular (Carrasco et al., 2003; Monaghan et al., 2005; Simmonds et al., 2003), the representation of which could be deficient in

coarse-resolution climate models. Therefore, future investigation is needed to evaluate model performance under various meteorological conditions as well as for other locations of the Antarctic continent.

This study finds that CAM6′s cloud fraction shows different signs of biases at lower and upper vertical levels, that is, the simulation underestimates cloud fraction below 3 km and overestimates cloud fraction above 3 km. The seasonal variations in cloud fraction biases are mostly within 0.1–0.2. Such vertical variations of cloud fraction bias is also well correlated with those seen in temperature, WVMR and RH. That is, positive (negative) biases of cloud fraction are correlated with positive (negative) biases of temperature, water vapor, and RH. Comparing the contributions of temperature and water vapor biases to the RH biases in vertical profiles, water vapor biases are the dominant contributor to both the magnitude and the direction of RH biases in vertical profiles. For these thermodynamic conditions, their seasonally averaged values are relatively similar, except for DJF with higher temperature and WVMR. The underestimation of low cloud fraction in CAM6 is possibly due to an adjustment to cloud fraction, which reduces the RH-derived low cloud fraction when the grid-box mean water vapor specific humidity is below 3 g/kg (also known as "freeze-dry") (Vavrus & Waliser, 2008). The altitudinal dependence of cloud fraction biases may also be partly due to CAM6 failing to represent the effects of katabatic flow seen in this region, as previously suggested for forecast and reanalysis models (e.g., Silber, Verlinde, Wang, et al., 2019; Wille et al., 2016). McMurdo Station is located close to multiple topographic features (Mount Erebus, Black and White Islands, etc.), which impact the mesoscale representation of lower tropospheric flow by radiosonde observation. Due to this limitation, simulated dynamical conditions are not evaluated in this work, while future investigation is warranted given their potential influences on cloud formation and moisture inflow.

Correlation analyses between cloud characteristics and thermodynamic conditions show important result for identifying the key factors contributing to model performance. RH is seen to affect cloud fraction biases, while WVMR bias is seen to be the primary driver of RH bias. Thus, these local results at McMurdo suggest that it may be important to improve estimation of WVMR in Antarctica, in order to reduce the biases of RH and cloud characteristics in the simulation. The misrepresentation of water vapor in the model originates in various parameterizations as well as the coarse model grid spacings. In the free troposphere, a combination of errors in the source of water vapor (e.g., remote convective detrainment, freeze drying in cirrus) and errors in transport and diffusion from the planetary boundary layer may lead to water vapor biases and smoothed out gradients. In addition, the fact that model cannot resolve the fine scale structure of water vapor in the atmosphere (particularly in the vertical) can also create errors. As a previous study pointed out, the lack of water vapor sub-grid variability in the CAM5 model likely leads to local dry biases and an underestimation of cloud fraction (Wu et al., 2017). A previous study that evaluated CAM6 against in situ observations over the Southern Ocean found that reducing temperature bias can also help to reduce moisture bias substantially (Gettelman et al., 2020). Future model development is recommended to examine the impacts of convective detrainment, freeze drying, and sub-grid scale parameterizations on water vapor biases as well as the correlation between temperature and water vapor biases.

The overestimation of liquid-containing cloud phase is consistent with several studies of phase partitioning using the DOE E3SM climate model based on ground-based and satellite observations (Rasch et al., 2019; M. Zhang et al., 2020; Y. Zhang, Xie, et al., 2019). Based on Arctic ground-based observations, M. Zhang et al. (2020) showed that two new parameterizations used in CAM6—the classical nucleation theory (CNT) and the CLUBB parameterizations—produce lower initial ice crystal number concentrations compared with the older version CAM5 model. CAM6 also uses MG2 cloud microphysics parameterization, which reduces the WBF process and lowers the conversion from liquid phase to ice compared with CAM5. Such change in the MG2 was found to have a smaller impact than those contributed by CNT and CLUBB. In addition, the current version of CAM6 does not include marine organic aerosols, which have been found to be an important type of INPs at 950 hPa over Antarctica and the Southern Ocean (Zhao et al., 2021). The lack of consideration of marine organic aerosols as INPs may also contribute to the lower occurrence frequency of ice phase at cloud fraction >0.6 shown in our evaluation of CAM6 at McMurdo Station. Since no INP measurements were provided by the AWARE campaign, acquiring additional observations of INPs in the future are recommended for this remote region in order to quantify the impacts of various types of INPs over Antarctica. Another study showed that the simulated IWC and ice crystal mean diameter in CAM6 are underestimated compared

with in situ observations, possibly due to weaker aerosol indirect effects and insufficient amounts of ice particle growth in the model (Patnaude et al., 2021). Therefore, to increase ice mass concentration and the amount of supercooled liquid water, further modifications are recommended for CNT, CLUBB and MG2 parameterizations, INP number concentrations and ice particle growth.

Caveats exist in this study due to the limitations in observational capabilities and the nature of numerical modeling. Remote sensing observations, while quality controlled, are subject to the influences of attenuation and sensitivity limits. Several methods are therefore used to evaluate simulated cloud phase, by including (Figures 8 and 9; S1–S3) or excluding the unknown phase (Figures 10 and 11) in the comparison. Radiosondes are limited by the number of releases possible, which provide fewer samples than ground-based remote sensing observations when analyzing collocated thermodynamic conditions and cloud characteristics. Furthermore, CAM6 was run on a coarser horizontal grid spacing than the observations. As the simulation was nudged toward MERRA-2 reanalysis data for temperature and 2-D horizontal wind, CAM6 temperature biases were found to largely originate from reanalysis data temperature biases. More evaluation on the representativeness of reanalysis data in Antarctica is out of the scope of this current work but recommended for future studies. Moreover, observations are either averaged to the coarse model grid scale (e.g., Figure 10), or the model output closest in time to the observations is repeatedly compared with multiple high-resolution observational data (Figures 8, 9 and 11). The two methods show similar results with each other, demonstrating the robustness of the model comparison results.

When comparing cloud fraction and cloud phase, the definitions of these quantities in the observations are dependent upon spatial scales, which may also affect the model evaluation results. For example, the combined lidar and radar retrievals at 10-s resolution show cloud fraction of either 0 or 1, while the averaged observations can have cloud fraction ranging from 0 to 1 (i.e., calculated as the number of in-cloud samples divided by the total number of samples at each pressure level). In addition, cloud phase of 10-s resolution observations is defined as either ice or liquid-containing phase, while by averaging observations onto coarser model grid scale, three cloud thermodynamic phases (i.e., ice, liquid and mixed) can be defined. Previous studies of in situ observations showed that mixed phase occurrence frequency increases when averaging the observations onto coarser spatial scales (D'Alessandro et al., 2019; Yang et al., 2020). Instrument sensitivities can also significantly affect the derived mixed-phase cloud occurrence frequency, as demonstrated by comparisons between spaceborne and ground-based radar observations (e.g., Silber et al., 2021). Thus, one should caution the spatial dependency of cloud phase distribution when comparing observations and model simulations at different spatial resolutions.

Representations of cloud characteristics in CAM6 can subsequently affect radiative forcing and precipitation. Cloud phase analysis shows ice and liquid phase occurrence frequencies normalized by total in-cloud samples being underestimated and overestimated, respectively. Given the fact that ice phase is more likely to sediment due to larger particle sizes compared with supercooled liquid water, the underestimation of ice phase in CAM6 may lead to an overestimation of cloud lifetime and an underestimation of precipitation. Quantifications of the impacts of these cloud fraction and cloud phase biases on cloud radiative effects and precipitation over Antarctica are suggested for future work. Overall, this work demonstrated several methods to facilitate the comparisons between various types of observations and GCM simulations by reconciling their differences in horizontal and vertical resolutions. The presented model biases in cloud characteristics and thermodynamic conditions can be used as a guidance for future parameterization development in the GCMs, specifically for extremely dry and cold conditions seen in the Antarctic region.

Data Availability Statement

Observation data are available from ARM Data Discovery (https://adc.arm.gov/discovery/). The CAM6 nudged simulation output around McMurdo Station are archived at data.mendeley.com under DOI: http://dx.doi.org/10.17632/x6n4r3yxb2.1.

References

Abbatt, J. P. D., Leaitch, W. R., Aliabadi, A. A., Bertram, A. K., Blanchet, J.-P., Boivin-Rioux, A., et al. (2019). Overview paper: New insights into aerosol and climate in the Arctic. *Atmospheric Chemistry and Physics*, *19*(4), 2527–2560. https://doi.org/10.5194/acp-19-2527-2019

Atlas, R. L., Bretherton, C. S., Blossey, P. N., Gettelman, A., Bardeen, C., Lin, P., & Ming, Y. (2020). How well do large-Eddy simulations and global climate models represent observed boundary layer structures and low clouds over the summertime southern Ocean? *Journal of Advances in Modeling Earth Systems*, *12*(11), e2020MS002205. https://doi.org/10.1029/2020MS002205

Bodas-Salcedo, A., Mulcahy, J. P., Andrews, T., Williams, K. D., Ringer, M. A., Field, P. R., & Elsaesser, G. S. (2019). Strong dependence of atmospheric feedbacks on mixed-phase microphysics and aerosol-cloud interactions in HadGEM3. *Journal of Advances in Modeling Earth Systems*, *11*(6), 1735–1758. https://doi.org/10.1029/2019MS001688

Bogenschutz, P. A., Gettelman, A., Morrison, H., Larson, V. E., Craig, C., & Schanen, D. P. (2013). Higher-order turbulence closure and its impact on climate simulations in the community atmosphere model. *Journal of Climate*, *26*(23), 9655–9676. https://doi.org/10.1175/JCLI-D-13-00075.1

Bromwich, D. H., Nicolas, J. P., Hines, K. M., Kay, J. E., Key, E. L., Lazzara, M. A., et al. (2012). Tropospheric clouds in Antarctica. *Reviews of Geophysics*, *50*(1), RG1004. https://doi.org/10.1029/2011RG000363

Carrasco, J. F., Bromwich, D. H., & Monaghan, A. J. (2003). Distribution and characteristics of mesoscale cyclones in the Antarctic: Ross Sea eastward to the Weddell Sea. *Monthly Weather Review*, *131*, 289–301. https://doi.org/10.1175/1520-0493(2003)131<0289:dacomc>2.0.co;2

Cesana, G., & Chepfer, H. (2013). Evaluation of the cloud thermodynamic phase in a climate model using CALIPSO-GOCCP. *Journal of Geophysical Research: Atmospheres*, *118*(14), 7922–7937. https://doi.org/10.1002/jgrd.50376

D'Alessandro, J. J., Diao, M., Wu, C., Liu, X., Jensen, J. B., & Stephens, B. B. (2019). Cloud phase and relative humidity distributions over the Southern Ocean in austral summer based on in situ observations and CAM5 simulations. *Journal of Climate*, *32*(10), 2781–2805. https://doi.org/10.1175/JCLI-D-18-0232.1

Danabasoglu, G., Lamarque, J. -F., Bacmeister, J., Bailey, D. A., DuVivier, A. K., Edwards, J., et al. (2020). The Community Earth System Model Version 2 (CESM2). *Journal of Advances in Modeling Earth Systems*, *12*(2), e2019MS001916. https://doi.org/10.1029/2019MS001916

de Boer, G., Eloranta, E. W., & Shupe, M. D. (2009). Arctic mixed-phase stratiform cloud properties from multiple years of surface-based measurements at two high-latitude locations. *Journal of the Atmospheric Sciences*, *66*(9), 2874–2887. https://doi.org/10.1175/2009JAS3029.1

Diao, M., Zondlo, M. A., Heymsfield, A. J., Avallone, L. M., Paige, M. E., Beaton, S. P., et al. (2014). Cloud-scale ice-supersaturated regions spatially correlate with high water vapor heterogeneities. *Atmospheric Chemistry and Physics*, *14*(5), 2639–2656. https://doi.org/10.5194/acp-14-2639-2014

Eloranta, E. E. (2006). High spectral resolution Lidar. In *Lidar* (pp. 143–163). Springer-Verlag. https://doi.org/10.1007/0-387-25101-4_5

Gettelman, A., Bardeen, C. G., McCluskey, C. S., Järvinen, E., Stith, J., Bretherton, C., et al. (2020). Simulating observations of southern Ocean clouds and implications for climate. *Journal of Geophysical Research: Atmospheres*, *125*(21), e2020JD032619. https://doi.org/10.1029/2020JD032619

Gettelman, A., & Morrison, H. (2015). Advanced two-moment bulk microphysics for global models. Part I: Off-line tests and comparison with other schemes. *Journal of Climate*, *28*(3), 1268–1287. https://doi.org/10.1175/JCLI-D-14-00102.1

Gettelman, A., Morrison, H., Santos, S., Bogenschutz, P., & Caldwell, P. M. (2015). Advanced two-moment bulk microphysics for global models. Part II: Global model solutions and aerosol–cloud interactions. *Journal of Climate*, *28*(3), 1288–1307. https://doi.org/10.1175/JCLI-D-14-00103.1

Golaz, J.-C., Larson, V. E., & Cotton, W. R. (2002a). A PDF-based model for boundary layer clouds. Part I: Method and model description. *Journal of the Atmospheric Sciences*, *59*(24), 3540–3551. https://doi.org/10.1175/1520-0469(2002)059<3540:APBMFB>2.0.CO;2

Golaz, J.-C., Larson, V. E., & Cotton, W. R. (2002b). A PDF-based model for boundary layer clouds. Part II: Model results. *Journal of the Atmospheric Sciences*, *59*(24), 3552–3571. https://doi.org/10.1175/1520-0469(2002)059<3552:APBMFB>2.0.CO;2

Guo, Z., Wang, M., Peng, Y., & Luo, Y. (2020). Evaluation on the vertical distribution of liquid and ice phase cloud fraction in community atmosphere model Version 5.3 using spaceborne Lidar observations. *Earth and Space Science*, *7*(3), e2019EA001029. https://doi.org/10.1029/2019EA001029

Hines, K. M., Bromwich, D. H., Wang, S.-H., Silber, I., Verlinde, J., & Lubin, D. (2019). Microphysics of summer clouds in central West Antarctica simulated by the Polar Weather Research and Forecasting Model (WRF) and the Antarctic Mesoscale Prediction System (AMPS). *Atmospheric Chemistry and Physics*, *19*(19), 12431–12454. https://doi.org/10.5194/acp-19-12431-2019

Hoose, C., Kristjánsson, J. E., Chen, J.-P., & Hazra, A. (2010). A classical-theory-based parameterization of heterogeneous ice nucleation by mineral dust, soot, and biological particles in a global climate model. *Journal of the Atmospheric Sciences*, *67*(8), 2483–2503. https://doi.org/10.1175/2010JAS3425.1

Iacono, M. J., Mlawer, E. J., Clough, S. A., & Morcrette, J.-J. (2000). Impact of an improved longwave radiation model, RRTM, on the energy budget and thermodynamic properties of the NCAR community climate model, CCM3. *Journal of Geophysical Research*, *105*(D11), 14873–14890. https://doi.org/10.1029/2000JD900091

Kay, J. E., Hillman, B. R., Klein, S. A., Zhang, Y., Medeiros, B., Pincus, R., et al. (2012). Exposing global cloud biases in the Community Atmosphere Model (CAM) using satellite observations and their corresponding instrument simulators. *Journal of Climate*, *25*(15), 5190–5207. https://doi.org/10.1175/JCLI-D-11-00469.1

Larson, V. E., Golaz, J.-C., & Cotton, W. R. (2002). Small-scale and mesoscale variability in cloudy boundary layers: Joint probability density functions. *Journal of the Atmospheric Sciences*, *59*(24), 3519–3539. https://doi.org/10.1175/1520-0469(2002)059<3519:SSAMVI>2.0.CO;2

Lawson, R. P., & Gettelman, A. (2014). Impact of Antarctic mixed-phase clouds on climate. *Proceedings of the National Academy of Sciences of the United States of America*, *111*(51), 18156–18161. https://doi.org/10.1073/pnas.1418197111

Li, Z., & Xu, K. (2020). Arctic clouds simulated by a multiscale modeling framework and comparisons with observations and conventional GCMs. *Journal of Geophysical Research: Atmospheres*, *125*(1), e2019JD030522. https://doi.org/10.1029/2019JD030522

Liou, K. N. (1992). *Radiation and cloud processes in the atmosphere*. Oxford University PressOxford University Press.

Liou, K. N., & Wittman, G. D. (1979). Parameterization of the radiative properties of clouds. *Journal of the Atmospheric Sciences*, *36*(7), 1261–1273. https://doi.org/10.1175/1520-0469(1979)036<1261:POTRPO>2.0.CO;2

Listowski, C., Delanoë, J., Kirchgaessner, A., Lachlan-Cope, T., & King, J. (2019). Antarctic clouds, supercooled liquid water and mixed phase, investigated with DARDAR: Geographical and seasonal variations. *Atmospheric Chemistry and Physics*, *19*(10), 6771–6808. https://doi.org/10.5194/acp-19-6771-2019

Listowski, C., & Lachlan-Cope, T. (2017). The microphysics of clouds over the Antarctic Peninsula–Part 2: Modelling aspects within Polar WRF. *Atmospheric Chemistry and Physics Discussions*, *17*, 1–41. https://doi.org/10.5194/acp-2016-1135

Liu, J., Dedrick, J., Russell, L. M., Senum, G. I., Uin, J., Kuang, C., et al. (2018). High summertime aerosol organic functional group concentrations from marine and seabird sources at Ross Island, Antarctica, during AWARE. *Atmospheric Chemistry and Physics*, *18*(12), 8571–8587. https://doi.org/10.5194/acp-18-8571-2018

Lubin, D., Zhang, D., Silber, I., Scott, R. C., Kalogeras, P., Battaglia, A., et al. (2020). AWARE: The Atmospheric Radiation Measurement (ARM) west Antarctic radiation experiment. *Bulletin of the American Meteorological Society*, *101*, E1069–E1091. https://doi.org/10.1175/BAMS-D-18-0278.1

Martin, D. F., Cornford, S. L., & Payne, A. J. (2019). Millennial-scale vulnerability of the Antarctic ice sheet to regional ice shelf collapse. *Geophysical Research Letters*, *46*(3), 1467–1475. https://doi.org/10.1029/2018GL081229

Matus, A. V., & L'Ecuyer, T. S. (2017). The role of cloud phase in Earth's radiation budget. *Journal of Geophysical Research: Atmospheres*, *122*(5), 2559–2578. https://doi.org/10.1002/2016JD025951

McErlich, C., McDonald, A., Schuddeboom, A., & Silber, I. (2021). Comparing satellite- and ground-based observations of cloud occurrence over high Southern latitudes. *Journal of Geophysical Research: Atmospheres*, *126*(6), 39. https://doi.org/10.1029/2020JD033607

Mioche, G., Jourdan, O., Ceccaldi, M., & Delanoë, J. (2015). Variability of mixed-phase clouds in the Arctic with a focus on the Svalbard region: A study based on spaceborne active remote sensing. *Atmospheric Chemistry and Physics*, *15*(5), 2445–2461. https://doi.org/10.5194/acp-15-2445-2015

Molod, A., Takacs, L., Suarez, M., & Bacmeister, J. (2015). Development of the GEOS-5 atmospheric general circulation model: Evolution from MERRA to MERRA2. *Geoscientific Model Development*, *8*(5), 1339–1356. https://doi.org/10.5194/gmd-8-1339-2015

Monaghan, A. J., Bromwich, D. H., Powers, J. G., & Manning, K. W. (2005). The climate of the McMurdo, Antarctica, region as represented by one year of forecasts from the Antarctic Mesoscale Prediction System. *Journal of Climate*, *18*(8), 1174–1189. https://doi.org/10.1175/JCLI3336.1

Morris, V. (2006). *Microwave Radiometer (MWR) Handbook*. https://doi.org/10.2172/1020715

Murphy, D. M., & Koop, T. (2005). Review of the vapour pressures of ice and supercooled water for atmospheric applications. *Quarterly Journal of the Royal Meteorological Society*, *131*(608), 1539–1565. https://doi.org/10.1256/qj.04.94

Neale, R. B., Richter, J. H., & Jochum, M. (2008). The impact of convection on ENSO: From a delayed oscillator to a series of events. *Journal of Climate*, *21*(22), 5904–5924. https://doi.org/10.1175/2008JCLI2244.1

Nicolas, J. P., Vogelmann, A. M., Scott, R. C., Wilson, A. B., Cadeddu, M. P., Bromwich, D. H., et al. (2017). January 2016 extensive summer melt in West Antarctica favoured by strong El Niño. *Nature Communications*, *8*(1), 15799. https://doi.org/10.1038/ncomms15799

Oppenheimer, M. (1998). Global warming and the stability of the West Antarctic Ice Sheet. *Nature*, *393*(6683), 325–332. https://doi.org/10.1038/30661

Patnaude, R., Diao, M., Liu, X., & Chu, S. (2021). Effects of thermodynamics, dynamics and aerosols on cirrus clouds based on in situ observations and NCAR CAM6. *Atmospheric Chemistry and Physics*, *21*(3), 1835–1859. https://doi.org/10.5194/acp-21-1835-2021

Ramanathan, V., Cess, R. D., Harrison, E. F., Minnis, P., Barkstrom, B. R., Ahmad, E., & Hartmann, D. (1989). Cloud-radiative forcing and climate: Results from the earth radiation budget experiment. *Science*, *243*(4887), 57–63. https://doi.org/10.1126/science.243.4887.57

Rasch, P. J., Xie, S., Ma, P. -L., Lin, W., Wang, H., Tang, Q., et al. (2019). An overview of the atmospheric component of the energy exascale earth system model. *Journal of Advances in Modeling Earth Systems*, *11*(8), 2377–2411. https://doi.org/10.1029/2019MS001629

Scott, R. C., & Lubin, D. (2016). Unique manifestations of mixed-phase cloud microphysics over Ross Island and the Ross Ice Shelf, Antarctica. *Geophysical Research Letters*, *43*(6), 2936–2945. https://doi.org/10.1002/2015GL067246

Scott, R. C., Lubin, D., Vogelmann, A. M., & Kato, S. (2017). West Antarctic ice sheet cloud cover and surface radiation budget from NASA a-train satellites. *Journal of Climate*, *30*(16), 6151–6170. https://doi.org/10.1175/JCLI-D-16-0644.1

Shepherd, A., Wingham, D., & Rignot, E. (2004). Warm Ocean is eroding West Antarctic Ice Sheet. *Geophysical Research Letters*, *31*(23), L23402. https://doi.org/10.1029/2004GL021106

Shi, X., Liu, X., & Zhang, K. (2015). Effects of pre-existing ice crystals on cirrus clouds and comparison between different ice nucleation parameterizations with the Community Atmosphere Model (CAM5). *Atmospheric Chemistry and Physics*, *15*(3), 1503–1520. https://doi.org/10.5194/acp-15-1503-2015

Shupe, M. D. (2011). Clouds at Arctic atmospheric observatories. Part II: Thermodynamic phase characteristics. *Journal of Applied Meteorology and Climatology*, *50*(3), 645–661. https://doi.org/10.1175/2010JAMC2468.1

Shupe, M. D., Uttal, T., & Matrosov, S. Y. (2005). Arctic cloud microphysics retrievals from surface-based remote sensors at SHEBA. *Journal of Applied Meteorology*, *44*(10), 1544–1562. https://doi.org/10.1175/JAM2297.1

Shupe, M. D., Walden, V. P., Eloranta, E., Uttal, T., Campbell, J. R., Starkweather, S. M., & Shiobara, M. (2011). Clouds at Arctic atmospheric observatories. Part I: Occurrence and macrophysical properties. *Journal of Applied Meteorology and Climatology*, *50*(3), 626–644. https://doi.org/10.1175/2010JAMC2467.1

Silber, I., Fridlind, A. M., Verlinde, J., Ackerman, A. S., Cesana, G. V., & Knopf, D. A. (2021). The prevalence of precipitation from polar supercooled clouds. *Atmospheric Chemistry and Physics*, *21*(5), 3949–3971. https://doi.org/10.5194/acp-21-3949-2021

Silber, I., Verlinde, J., Cadeddu, M., Flynn, C. J., Vogelmann, A. M., & Eloranta, E. W. (2019). Antarctic cloud macrophysical, thermodynamic phase, and atmospheric inversion coupling properties at McMurdo station—Part II: Radiative impact during different synoptic regimes. *Journal of Geophysical Research: Atmospheres*, *124*(3), 1697–1719. https://doi.org/10.1029/2018JD029471

Silber, I., Verlinde, J., Eloranta, E. W., & Cadeddu, M. (2018). Antarctic cloud macrophysical, thermodynamic phase, and atmospheric inversion coupling properties at McMurdo station: I. principal data processing and climatology. *Journal of Geophysical Research: Atmospheres*, *123*(11), 6099–6121. https://doi.org/10.1029/2018JD028279

Silber, I., Verlinde, J., Wang, S.-H., Bromwich, D. H., Fridlind, A. M., Cadeddu, M., et al. (2019). Cloud influence on ERA5 and AMPS surface downwelling longwave radiation biases in West Antarctica. *Journal of Climate*, *32*(22), 7935–7949. https://doi.org/10.1175/JCLI-D-19-0149.1

Silber, I., Verlinde, J., Wen, G., & Eloranta, E. W. (2020). Can embedded liquid cloud layer volumes be classified in polar clouds using a single- frequency Zenith-pointing radar? *IEEE Geoscience and Remote Sensing Letters*, *17*(2), 222–226. https://doi.org/10.1109/LGRS.2019.2918727

Simmonds, I., Keay, K., & Lim, E. P. (2003). Synoptic activity in the seas around Antarctica. *Monthly Weather Review*, *131*, 272–288. https://doi.org/10.1175/1520-0493(2003)131<0272:saitsa>2.0.co;2

Turner, J., Lachlan-Cope, T. A., Colwell, S., Marshall, G. J., & Connolley, W. M. (2006). Significant warming of the Antarctic winter troposphere. *Science (New York, N.Y.)*, *311*(5769), 1914–1917. https://doi.org/10.1126/science.1121652

Vavrus, S., & Waliser, D. (2008). An improved parameterization for simulating Arctic cloud amount in the CCSM3 Climate Model. *Journal of Climate*, *21*(21), 5673–5687. https://doi.org/10.1175/2008JCLI2299.1

Wang, M., Liu, X., Zhang, K., & Comstock, J. M. (2014). Aerosol effects on cirrus through ice nucleation in the Community Atmosphere Model CAM5 with a statistical cirrus scheme. *Journal of Advances in Modeling Earth Systems*, 6(3), 756–776. https://doi.org/10.1002/2014MS000339

Webb, M. J., Andrews, T., Bodas-Salcedo, A., Bony, S., Bretherton, C. S., Chadwick, R., et al. (2017). The Cloud Feedback Model Intercomparison Project (CFMIP) contribution to CMIP6. *Geoscientific Model Development*, 10(1), 359–384. https://doi.org/10.5194/gmd-10-359-2017

Widener, K., Bharadwaj, N., & Johnson, K. (2012). *Ka-Band ARM Zenith Radar (KAZR) Instrument Handbook*. https://doi.org/10.2172/1035855

Wille, J. D., Bromwich, D. H., Nigro, M. A., Cassano, J. J., Mateling, M., Lazzara, M. A., & Wang, S. H. (2016). Evaluation of the AMPS boundary layer simulations on the Ross Ice Shelf with tower observations. *Journal of Applied Meteorology and Climatology*, 55(11), 2349–2367. https://doi.org/10.1175/JAMC-D-16-0032.1

Wu, C., Liu, X., Diao, M., Zhang, K., Gettelman, A., Lu, Z., et al. (2017). Direct comparisons of ice cloud macro- and microphysical properties simulated by the Community Atmosphere Model version 5 with HIPPO aircraft observations. *Atmospheric Chemistry and Physics*, 17(7), 4731–4749. https://doi.org/10.5194/acp-17-4731-2017

Yang, C., Diao, M., Gettelman, A., Zhang, K., & Sun, J. (2020). Ice and Supercooled Liquid Water Distributions over the Southern Ocean based on In Situ Observations and Climate Model Simulation. *Earth and Space Science Open Archive*. https://doi.org/10.1002/essoar.10504450.1

Zelinka, M. D., Myers, T. A., McCoy, D. T., Po-Chedley, S., Caldwell, P. M., Ceppi, P., et al. (2020). Causes of higher climate sensitivity in CMIP6 models. *Geophysical Research Letters*, 47(1), e2019GL085782. https://doi.org/10.1029/2019GL085782

Zhang, D., Vogelmann, A., Kollias, P., Luke, E., Yang, F., Lubin, D., & Wang, Z. (2019). Comparison of Antarctic and Arctic single-layer stratiform mixed-phase cloud properties using ground-based remote sensing measurements. *Journal of Geophysical Research: Atmospheres*, 124(17–18), 10186–10204. https://doi.org/10.1029/2019JD030673

Zhang, G. J., & McFarlane, N. A. (1995). Sensitivity of climate simulations to the parameterization of cumulus convection in the Canadian climate centre general circulation model. *Atmosphere-Ocean*, 33(3), 407–446. https://doi.org/10.1080/07055900.1995.9649539

Zhang, K., Wan, H., Liu, X., Ghan, S. J., Kooperman, G. J., Ma, P.-L., et al. (2014). Technical Note: On the use of nudging for aerosol–climate model intercomparison studies. *Atmospheric Chemistry and Physics*, 14(16), 8631–8645. https://doi.org/10.5194/acp-14-8631-2014

Zhang, M., Liu, X., Diao, M., D'Alessandro, J. J., Wang, Y., Wu, C., et al. (2019). Impacts of representing heterogeneous distribution of cloud liquid and ice on phase partitioning of Arctic mixed-phase clouds with NCAR CAM5. *Journal of Geophysical Research: Atmospheres*, 124(23), 13071–13090. https://doi.org/10.1029/2019JD030502

Zhang, M., Xie, S., Liu, X., Lin, W., Zhang, K., Ma, H., et al. (2020). Toward understanding the simulated phase partitioning of Arctic single-layer mixed-phase clouds in E3SM. *Earth and Space Science*, 7(7), e2020EA001125. https://doi.org/10.1029/2020EA001125

Zhang, Y., Xie, S., Lin, W., Klein, S. A., Zelinka, M., Ma, P., et al. (2019). Evaluation of clouds in version 1 of the E3SM atmosphere model with satellite simulators. *Journal of Advances in Modeling Earth Systems*, 11(5), 1253–1268. https://doi.org/10.1029/2018MS001562

Zhao, X., Liu, X., Burrows, S. M., & Shi, Y. (2021). Effects of marine organic aerosols as sources of immersion-mode ice-nucleating particles on high-latitude mixed-phase clouds. *Atmospheric Chemistry and Physics*, 21(4), 2305–2327. https://doi.org/10.5194/acp-21-2305-2021

Erratum

Figure 1 has been updated since this paper originally published. The color bar for Figure 1C has been updated to include the previously missing gray bar. The gray color shows unknown phase. The updated figure may be considered the version of record.